A SPECTROSCOPIC STUDY OF IMPURITY BEHAVIOR IN NEUTRAL-BEAM AND OHMICALLY HEATED TFTR DISCHARGES

PPPL--2410

DE87 008073

B.C. Stratton, A.T. Ramsey, F.P. Boody, C.E. Bush†,
R.J. Fonck, R.J. Groebner*, R.A. Hulse, R.K. Richards†,
and J. Schivell

Princeton Plasma Physics Laboratory
Princeton, New Jersey 08544

† permanent address: Oak Ridge National Laboratory,
Oak Ridge, TN

* permanent address: GA Technologies Inc.,
San Diego, CA

DISCLAIMER

DISCLAIMER

Portions of this document may be illegible in electronic image products. Images are produced from the best available original document.

ABSTRACT

Quantitative spectroscopic measurements of Z_{eff}, impurity densities, and radiated power losses have been made for ohmic- and neutral-beam-heated TFTR discharges at a plasma current of 2.2 MA and toroidal field of 4.7 T. Variations in these quantities with line-average plasma density ($\bar{n}_e$) and beam power up to 5.6 MW are presented for discharges on a graphite movable limiter. A detailed discussion of the use of an impurity transport model to infer absolute impurity densities and radiative losses from line intensity and visible continuum measurements is given. These discharges were dominated by low-Z impurities with carbon having a considerably higher density than oxygen, except in high-$\bar{n}_e$ ohmic discharges, where the densities of carbon and oxygen were comparable. Metallic impurity concentrations and radiative losses were small, resulting in hollow radiated power profiles and fractions of the input power radiated being 30-50% for ohmic heating and 30% or less with beam heating. Spectroscopic estimates of the radiated power were in good agreement with bolometrically measured values. Due to an increase in the carbon density, Z_{eff} rose from 2.0 to 2.8 as the beam power increased from 0 to 5.6 MW, pointing to a potentially serious dilution of the neutron-producing plasma ions as the beam power increased. Both the low-Z and metallic impurity concentrations were approximately constant with minor radius, indicating no central impurity accumulation in these discharges.

I. Introduction

The study of impurity production and behavior in tokamak plasmas continues to be a topic of considerable importance in fusion research. Mid-sized tokamaks with intense auxiliary heating have produced fusion-grade plasmas with minimal power losses due to impurity radiation (for a summary see the review of Isler [1]), except in some enhanced confinement regimes where catastrophic impurity accumulation occurs [2,3]. With the advent of high-power heating experiments on the current generation of large tokamaks such as TFTR, JET, and JT-60, a re-examination of impurity behavior is necessary. Even when radiative losses are unimportant compared to the central heating power, modifications of the edge plasma (which may play a role in enhanced confinement scenarios) due to impurity radiation and dilution of the fusion fuel are topics of primary importance as breakeven conditions are approached in these devices.

This paper presents a detailed analysis of extreme UV and visible impurity emissions from TFTR plasmas on a graphite movable limiter with up to 5.6 MW of beam power. It provides reference documentation of both ohmic and standard beam-heated (L-mode confinement) discharges, with other TFTR operating regimes, such as the high ion-temperature, beam-heated discharges and high-density, pellet-fuelled plasmas left to future study. In this spirit, the techniques used to analyze extreme UV and visible impurity emissions from TFTR plasmas are discussed in detail. As a further focus, variations in impurity behavior with density and beam power in discharges with 2.2 MA plasma current (I_p) and 4.7 T toroidal field (B_T) are discussed in detail. In addition to this paper, which concentrates on extreme UV and visible spectroscopic observations, a study of impurities in earlier TFTR ohmic plasmas based primarily on soft x-ray pulse-height analysis measurements has been given by Hill et al. [4].

The second section of this paper describes the relevant regime of TFTR operation and the spectroscopic diagnostics used. The following section discusses in detail the quantitative analysis of line-integrated spectroscopic measurements using an impurity transport code. A study of the sensitivity of this analysis to the assumptions made regarding impurity transport and edge plasma parameters, important given the size and high temperature of TFTR plasmas, is also given in the third section. The fourth section presents the

results of using these analysis procedures to study variations in impurity behavior in ohmic- and beam-heated plasmas as the plasma density and beam power are varied.

II. TFTR Operating Conditions and Spectroscopic Diagnostics

During the two-neutral-beam period of TFTR operation (September 1984 - April 1985), significant plasma ion and electron heating was achieved by neutral beam injection with energies up to 80 keV and power levels up to 6 MW. During this period TFTR was operated with B_T and I_p up to 5.2 T and 2.5 MA, respectively. Detailed descriptions of this period of TFTR operation with an emphasis on confinement results are given elsewhere [5,6]; we briefly note some relevant parameters of the discharges studied here.

The plasmas discussed here had a major radius of 255-259 cm and a minor radius of 82 cm. A movable graphite blade limiter located on the large major radius side of the plasma at one toroidal location was the primary limiter; as a result, carbon was usually the dominant impurity species. The other important low-Z impurity in the plasma was oxygen desorbed from both the vacuum vessel walls and the limiter [7]. The quantity of oxygen present in a given discharge depended upon how recently chromium gettering had been performed [7], as well as the history of machine conditioning and plasma operation. The discharge-cleaning techniques used to condition the vacuum vessel, and its long-term clean-up due to plasma operation, have been described by LaMarche et al. [8]. The vacuum vessel is stainless steel, with Inconel cover plates located on the large major radius side of the torus near the midplane to protect the vacuum vessel bellows from accidental contact with the plasma. The small major radius wall of the vacuum vessel in the vicinity of the midplane was covered with Inconel slats which served as a preliminary inner bumper limiter. Although the plasmas discussed here were in direct contact only with the movable limiter, the close proximity of the plasma periphery to the Inconel inner bumper limiter and the Inconel bellows cover plates resulted in the major metallic impurities in the plasma being nickel and chromium, the primary constituents of Inconel. Smaller amounts of iron and titanium were also observed, the iron coming from the stainless steel vacuum vessel and from the Inconel components and the titanium remaining from a TiC coating previously deposited on the graphite limiter and removed before

the period of operation discussed here. Metallic impurities are believed to enter the plasma primarily by sputtering of material deposited on the graphite limiter during pulse discharge cleaning and disruptions [4].

Two co-tangential neutral beam injectors were used during this run period. Each injector produced three independent beams which had different tangency radii. The sources operated with a primary energy component of approximately 80 keV. The beam energy distribution was fairly broad with approximately half of the power at the full energy. The beam pulses were 0.5 sec long. For the discharges discussed here, both the injected species and the target plasma were deuterium.

The primary spectroscopic impurity diagnostics on TFTR consist of two grazing-incidence multichannel spectrographs for line emission measurements and an array of filtered detectors used to measure the poloidal distribution of visible bremsstrahlung radiation.

Impurity line emissions in the 100-1100 Å range were observed using the SPRED survey spectrograph [9], which has a radial line-of-sight in the plasma midplane. A 450 g/mm grating, which covers the 100-1100 Å range with 2 Å (FWHM) spectral resolution, was used. The detector is an image-intensified 1024-channel photodiode array. Detector integration times of 50-100 ms were used. SPRED has been radiometrically calibrated over its entire wavelength range using synchrotron radiation from the National Bureau of Standards SURF II electron storage ring [10], with an estimated accuracy of ± 30%. A SPRED spectrum of the 100-1100 Å region during an ohmic TFTR discharge is shown in Fig. 1. This discharge, which will be discussed in the following section as an example of the data analysis procedure, had I_p = 2.2 MA, B_T = 4.7 T, and a line average electron density ($\bar{n}_e$) of 3.6 x 10^{13} cm^{-3} at 3.35 sec, the time of the spectrum shown in Fig. 1. (Because the sensitivity of the instrument varies by two orders of magnitude over the range 100-1100 Å, the longer wavelength lines of carbon and oxygen are brighter than the short wavelength metal lines.) As seen in Fig. 1, the 100-1100 Å region contains many lines from ionization states up to LiI-like of low-Z and metallic impurity elements.

The SOXMOS spectrograph [11] was used to observe line radiation in the 10-320 Å region. This 2-meter grazing-incidence (88.5° angle) instrument utilizes a 600 g/mm grating and an image-intensified photodiode array detector with typical integration times of 50-100 ms. The detector may be positioned

on the Rowland circle to observe a particular wavelength range during a discharge. The instrument line-of-sight is radial and lies in the horizontal midplane of the torus. SOXMOS was absolutely calibrated over most of its wavelength range through a two-step process. The calibration in the 100-320 Å region was accomplished by transfer of the SPRED calibration during TFTR discharges using lines from high ionization states of metallic impurity elements, which have distributions that should be toroidally and poloidally symmetric. Calibration points at 16 Å and 28.5 Å were obtained using the CVI 182 Å - 28.5 Å and OVIII 102 Å - 16 Å branching ratios. Recombination of fully ionized carbon and oxygen due to charge exchange with thermal neutrals can contribute significantly to the populations of the upper levels (n = 3) of these transitions and result in excited state populations considerably different from those expected from electron impact excitation from the ground state. The branching ratios were, therefore, not exactly equal to the ratio of transition probabilities and had to be evaluated with the MIST impurity transport code using thermal neutral densities calculated by the DEGAS code [12] and the cascade-corrected charge exchange recombination rates of Fonck, et al. [13]. As a result of this effect, the accuracy of the short wavelength calibration is probably not better than 50%. The sensitivity at the wavelengths of the important HI-like carbon and oxygen transitions, CVI 34 Å and OVIII 19 Å, was determined by linear interpolation. Figure 2 shows a spectrum of the 15 - 36 Å region, which contains several resonance lines of HI and HeI-like carbon and oxygen, from the example discharge.

Visible bremsstrahlung emission at 5235 Å was measured using the HAIFA diagnostic [14], which consists of a poloidal array of 18 detectors viewing the region ± 50° above and below the horizontal midplane of the torus and allowing a view of the entire diameter of an 82 cm minor radius plasma. Each channel consists of a telescope which views a chord through the plasma, a fiber optic link between the telescope and detector, and a detector composed of a pair of interference filters and a photomultiplier tube. The system has been absolutely calibrated using a National Bureau of Standards calibrated tungsten filament lamp. Z_{eff} profiles were obtained from the smoothed and Abel-inverted array data, n_e and T_e radial profiles obtained from Thomson scattering measurements, a far-infrared laser interferometer system (n_e), or electron-cyclotron-emission measurements (T_e), and the appropriate free-free transition Gaunt factor [14]. A simpler "Z-meter" method of analysis in which

a Z_{eff} averaged across the plasma diameter was obtained from data from one channel with a line-of-sight in the horizontal midplane was also used. Because the Z_{eff} profiles were approximately flat in the discharges discussed here, this method yielded a Z_{eff} characteristic of the entire core plasma volume. (Z_{eff} profiles for ohmic- and beam-heated discharges are discussed in section IV.) The Z_{eff} obtained by the Z-meter method is generally in agreement with the central value obtained from the array data. For the discharges discussed here, visible bremsstrahlung Z_{eff} measurements were in good agreement with those from neoclassical resistivity calculations and soft x-ray pulse-height analysis [15].

III. Impurity Transport Modelling and Sensitivity Analysis

The goal of the data analysis procedure is to obtain absolute densities of all important impurity species present in the plasma, their contributions to Z_{eff}, and the power radiated by each impurity element. For metallic impurities, these quantities are reliably obtained by MIST (Multi-Ionic Species Transport) code [16] modelling of the measured line brightnesses. For low-Z impurities such as carbon and oxygen, modelling of line brightnesses to obtain impurity densities is unreliable because these elements are fully ionized over almost the entire plamsa volume. As a result, low-Z impurity line emission excited by electron collisions originates primarily from the plasma periphery ($r/a \gtrsim 0.8$) and the scrape-off region, where T_e, n_e, the thermal neutral density, and impurity transport and sources, which are required by the code, are poorly known. However, it is possible to obtain the carbon-to-oxygen density ratio by modelling the brightnesses of the 1s - 2p transitions in the HI-like ions of these elements. The $\Delta n = 1$ transitions in the LiI-like ions may also be used for this purpose. The principle of this measurement is that the intensities of these lines are proportional to the flux of impurity ions via the ratio of ionization to excitation rates [1]; assuming similar impurity transport, the ratio of carbon to oxygen fluxes in a given ionization state is equal to the carbon-to-oxygen density ratio. Absolute carbon and oxygen densities are then found from the measured Z_{eff} by subtracting the contribution of the metals and alloting the remainder to carbon, oxygen, and deuterons according to the measured carbon-to-oxygen density ratio. The power radiated by oxygen and carbon is obtained by using MIST to model the resulting carbon and oxygen densities. Since these radiated

power calculations are sensitive to the edge plasma parameters mentioned above, the spectroscopic total radiated power is checked for consistency with bolometer-radiated power measurements. Following a brief description of the MIST code (see ref. 16 for details), analysis of the data shown in Figs. 1 and 2 is given as an example of these procedures.

For a given impurity element the MIST code solves the impurity continuity equations

$$\frac{\partial n_q}{\partial t} = \frac{-1}{r}\frac{\partial}{\partial r}(r\Gamma_q) + I_{q-1}\,n_{q-1} - (I_q + R_q)n_q + R_{q+1}n_{q+1} - n_q/\tau_q + S_q, \quad (1)$$

where the index q, which runs from zero to the nuclear charge of the element, indicates the ionization state of the impurity. Γ_q is the radial particle flux density, n_q is the particle density, I_q is an ionization rate, R_q is a recombination rate, τ_q is a confinement time describing parallel loss to the limiter of ions in the scrape-off region of the plasma, and S_q describes the impurity volume source (usually $S_q = 0$ for $q \neq 0$). Electron impact ionization together with radiative, dielectronic, and charge exchange recombination are included. Except for the neutral impurity deposition calculation, impurity density radial distributions are assumed to be poloidally and toroidally symmetric.

Measured T_e and n_e profiles and calculated thermal and beam neutral particle energies and densities are input into the code. Depending on the time during the discharge to be analyzed, T_e profiles are taken from measurements by Thomson scattering or one of two electron-cyclotron-emission diagnostics: the Michelson interferometer ($2\omega_{ce}$) or the fast scanning radiometer (ω_{ce}), and n_e profiles are obtained from Thomson scattering or a far-infrared laser interferometer (MIRI). The profiles are smoothed and symmetrized before input into MIST. The thermal and beam neutral data are calculated using the time-independent, snapshot radial-profile analysis (SNAP) code [17]. For the example discharge, Fig. 3 shows the T_e profile from Thomson scattering and the n_e profile from MIRI at 3.35 sec.

Γ_q is taken to have the form

$$\Gamma_q = \frac{-D\partial n_q(r)}{\partial r} + v(r)n_q(r), \quad (2)$$

where D is a diffusion coefficient assumed to be constant as a function of minor radius, and v(r) is a convective velocity. For simplicity, D and v(r) are assumed to be the same for all ionization states of the impurity element. D is usually taken to be 10^4 cm^2/s, a value obtained in MIST modelling of emissions from germanium injected into TFTR discharges similar to those discussed here [18]. The intrinsic impurity analysis is usually insensitive to the exact value of D used in the model.

The convective velocity is parameterized in one of two ways [19]:

$$v(r) = -c_v \frac{2D}{a} r/a, \text{ or} \quad (3)$$

$$v(r) = c_v D \frac{\partial \ln[n_e(r)]}{\partial r}, \quad (4)$$

where c_v is a constant parameter which is related to the degree of central peaking of the impurity density profile. For equilibrium solutions to equations (1) ($\partial n_q/\partial t = 0$ for all q), v(r)/D is simply related to the shape of $n_z(r)$, the total impurity density profile ($n_z = \sum_{q=1}^{Z} n_q$) in the source/sink-free plasma region [19]. Since D is assumed to be constant, the shape of this transport equilibrium impurity density profile is determined by the functional form of v(r). If equation (3) is used, $n_z(r)$ has the shape of a gaussian to the c_v power. If equation (4) is used, $n_z(r)$ has the shape of $n_e(r)^{c_v}$. For most of the present work, equation (4) was used with c_v equal to one, i.e., the total impurity density profile was assumed to have the shape of the electron density profile. The flat Z_{eff} profiles measured in discharges similar to those discussed here and the metallic impurity modelling described below support this choice.

A simple neutral impurity model is used to provide a source of singly ionized impurity atoms in equations (1). Monoenergetic neutral atoms are launched from a specified source radius with an inwardly directed velocity and are ionized by electron impact. The scrape-off region T_e and n_e profiles are specified by scale lengths for these parameters whose values are estimated from probe measurements in similar discharges [20]; typical values were 2 cm for the n_e scale length and 6 cm for the T_e scale length. The scrape-off region parallel confinement time, τ, in equations (1) is parameterized as λ^2/D, where λ is a scale length which determines the effective distance of the

particle sink from the limiter radius [19]. λ was assumed to be 5 cm in the present work.

For metallic impurities and carbon, the source radius is assumed to be the limiter radius, 82 cm, while for oxygen it is assumed to be the wall radius. Since the plasma is not centered in the vacuum vessel, the wall radius is not unique, and a value of 90 cm is used in the code. The use of a larger value does not produce significantly different results because n_e and T_e are small at minor radii larger than 90 cm. Chromium gettering experiments indicate that approximately equal amounts of oxygen are produced at the limiter and vacuum vessel walls [7]. The neutral particle initial energy is taken to be 1 eV. The values of the edge parameters significantly affect the results only for the lowest ionization states, particularly those existing in the scrape-off region. This is one reason why emissions from the HI-like ionization states of carbon and oxygen, which originate inside the limiter radius, are preferred for measurement of the carbon-to-oxygen density ratio.

Once the radial distributions of the ionization states of an element have been calculated by solution of equations (1), the brightnesses of the observed lines are calculated using the coronal assumption of excitation of the upper level of a transition by electron impact and de-excitation by radiative decay. The electron-impact excitation rates of Mewe [21] are typically used; where possible, the accuracy of these rates is checked by comparison with more sophisticated calculations. For the 1s-2p transitions of CVI and OVIII, population of the n = 2 level due to cascading from higher n levels populated by thermal neutral and, where applicable, beam-neutral charge exchange recombination is included [13]. Total radiated power losses are calculated using radiative cooling rates calculated for each charge state [22] combined with the transport equilibrium ionization balance from equations (1). The calculated line brightnesses are then compared with the measured values and, if necessary, c_v is varied until the ratio of calculated and measured brightnesses for all observed lines agrees.

Tables I and II show the results of the metallic impurity analysis for the example discharge. The nickel and chromium lines used are listed in Table I along with their measured and calculated brightnesses. Because iron and titanium densities are measured to be considerably lower than those of chromium and nickel, these elements are usually not considered in the

analysis. The lines emitted by the MgI-, NaI-, BeI-, and LiI-like ionization states were chosen because they are strong and because the relatively simple atomic structure of these ions (one or two electrons outside a closed shell) allows reliable calculation of the electron impact excitation rates. The NiXXV 118 Å line is blended with strong lines of NiXXII and NIXXIV, and based on calculated relative intensities of the lines [23], the measured brightness of this blend at 118 Å is multiplied by 0.6 to obtain the brightness of the NiXXV line. The CrXXI 150 Å line (BeI-like) was not used because it is blended with the bright OVI 150 Å line. In high density discharges the metallic impurity lines are weak compared to the low-Z impurity lines and some of the lines become blended with carbon and oxygen lines; in such instances, these lines are omitted from the analysis. The calculated brightnesses in Table I assume the central impurity densities given in Table II: 1.1×10^9 cm^{-3} for Ni and 9.0×10^8 cm^{-3} for Cr.

The convective velocity was taken to have the form of equation (4) with $c_v = 1.0$, yielding constant metallic impurity concentration (fraction of n_e) profiles. Brightnesses of nickel lines emitted from significantly different radii provide a constraint on the shape of the metallic impurity density profiles. Figure 4 shows the calculated radial distribution of the higher ionization states of nickel for the example discharge. The NiXXV and NiXXVI lines are primarily emitted from minor radii less than 40 cm, while the NiXVII and NiXVIII lines are emitted from the region between 65 cm and 75 cm. As seen in Table I, the measured and calculated brightnesses of lines from all these ions agree well, within 35% or better; thus, the assumption that the nickel concentration profile is flat is approximately correct. The same procedure is used in the chromium analysis. In general, a flat metallic impurity concentration profile gives good agreement between the measured and calculated line brightnesses. Table II shows that metallic impurities contribute little to Z_{eff} and the total radiated power.

As mentioned earlier, MIST is also used to infer the central carbon-to-oxygen density ratio from ratios of measured brightnesses of $\Delta n = 1$ transitions in the HI- and LiI-like ions. A study was made to determine the sensitivity of this measurement to values of various plasma parameters and transport parameters which are input into the code (see, also, the discussion of Hawryluk et al. [24]). The results are summarized in Table III, where

brightnesses of several $\Delta n = 1$ transitions in the HI- and LiI-like ions of carbon and oxygen, CVI 34 Å, OVIII 19 Å, CIV 384 Å, and OVI 173 Å, calculated for the example discharge are listed. Central concentrations of both impurities were assumed to be 0.1% of $n_e(0)$. Also listed are the CVI 34 Å/OVI 19 Å and CIV 384 Å/OVI 173 Å brightness ratios. The reference values were calculated using the nominal values of the plasma parameters for the discharge. The value of each parameter was independently increased and decreased by a factor of two. The following parameters were varied: the neutral impurity atom source energy, the source minor radius, the scrape-off layer T_e and n_e scale lengths, λ, D, c_v, the thermal neutral density, T_e, n_e, the ionization rates, and the recombination rates. The variations in T_e and n_e were intended to simulate uncertainties in the edge values of these parameters, not in the values for minor radii less than approximately 70 cm, which are well known. Table III shows that, although the brightnesses change significantly as these parameters are varied, the brightness ratios are not strongly affected. This is particularly true for the CVI 34 Å/OVIII 19 Å ratio, which varies by less than 50% from the reference value. Because these lines are emitted from inside the limiter radius, this ratio is not as sensitive to variations of the edge parameters as the CIV 384 Å/OVI 173 Å ratio. Note that if the latter ratio were calculated assuming a carbon source radius of 82 cm and an oxygen source radius of 90 cm, its value would be smaller by a factor of two. This represents the situation of the limiter being the carbon source and the wall being the oxygen source. The final experimental uncertainty in the carbon-to-oxygen density ratio deduced from the HI-like line brightnesses is approximately a factor of two: 50% from the modelling and 50% from the uncertainty in the relative sensitivity of SOXMOS at these short wavelengths.

Table IV shows the results of the low-Z impurity analysis for the example discharge. Central impurity densities of 0.1% $n_e(0)$ were assumed in calculating the line brightnesses. For either the HI- or LiI-like ions, the ratio of brightness ratios listed in the far right-hand column is the central carbon-to-oxygen density ratio. This ratio is 10.3 using the HI-like ions and is 8.6 using the average of the values from the LiI-like ions. These measurements generally agree within a factor of two; when the discrepancy is significant, the more reliable value from the HI-like ions is used.

The central carbon, oxygen, and deuteron densities were obtained from the

carbon-to-oxygen density ratio, the metallic impurity densities, Z_{eff}, and $n_e(0)$. The results given in Table II were calculated using the carbon-to-oxygen density ratio from the HI-like ions. The carbon and oxygen concentrations obtained by modelling the line brightnesses directly were lower than these values by a factor of approximately 2.5 and were clearly inconsistent with the measured Z_{eff}. Table II shows that carbon was the major contributor to Z_{eff} in this discharge, and that, as a result of dilution of the working gas by impurities, the deuteron concentration was 72%. Because the contribution of carbon to the total Z_{eff} was greater than or equal to that of oxygen in the discharges considered here, the deduced oxygen densities were more sensitive than the carbon densities to uncertainties in the carbon-to-oxygen density ratio. Since this ratio was not measured to better than a factor of two, the absolute oxygen densities were uncertain by approximately this amount in many cases.

The central radiated power density and the total power radiated by carbon and oxygen obtained from MIST modelling are given in Table II. The total radiated power measured by spectroscopy was 640 kW, in excellent agreement with the bolometer measurement of 705 kW. Spectroscopic and bolometric radiated power profiles are compared in Fig. 5. The spectroscopic profile includes contributions from carbon, oxygen, nickel, and chromium. Agreement is quite good. The radiated power profile was hollow, as expected when carbon and oxygen are the major impurities. It is interesting to note that the central radiated power density was primarily due to carbon and oxygen radiation; low-Z impurity densities were sufficiently higher than those of metallic impurities that bremsstrahlung from electron collisions with low-Z impurities dominated line emission from metallic impurities in the plasma core. (By comparison, bremmstrahlung emitted by electron-deuteron collisions yielded 1.1 mW/cm^3 radiated power on axis.)

IV. Impurity Behavior in Neutral-Beam-Heated and Ohmic Discharges

1. Time Evolution During a Neutral-Beam-Heated Discharge

This section examines the time evolution of Z_{eff}, impurity densities, and radiative losses during a beam-heated discharge. Figure 6 shows the time evolution of $\bar{n}_e$ during a discharge with 5.6 MW beam power, I_p = 2.2 MA, and B_T

= 4.7 T. Beam injection started at 2.8 sec and ended at 3.3 sec; $\bar{n}_e$ rose from 3.1 x 10^{13} cm^{-3} at 2.75 sec, immediately before beam injection, to 4.6 x 10^{13} cm^{-3} at 3.25 sec, just before the end of beam injection. The density rise with beam injection was due to beam particle fueling [5]; its magnitude increased with beam power. Z_{eff} from the Z-meter analysis decreased from 3.6 before beam injection to 2.8 at the end of the beam pulse; this decrease was almost proportional to the $\bar{n}_e$ rise, indicating little or no change in the dominant impurity density with beam injection. Figure 7 shows the Z_{eff} profile from this discharge at 3.25 sec; also shown is the Z_{eff} profile from an ohmic discharge at the same I_p, B_T, and $\bar{n}_e$. Within the accuracy of the Abel inversion procedure and the peripheral n_e measured by Thomson scattering, the profile was flat in both cases.

Line emissions from all impurity species increased with neutral beam injection, as shown by the time evolution of the brightnesses of several lines shown in Fig. 8. The brightnesses of the CVI and OVIII lines reached approximately constant levels before the end of the beam pulse, while those of the metallic impurities increased throughout the beam pulse. These line brightness increases were due to a combination of changes in impurity densities, n_e, T_e, and beam and thermal neutral densities.

Impurity densities before and during beam heating in this discharge are shown in Table V. Metallic impurity densities increased by more than a factor of two with beam injection; such an increase is always seen on TFTR. However, the total metallic impurity concentrations were small, approximately 0.01% both before and during beam heating, and made negligible contributions to the total Z_{eff}.

The carbon-to-oxygen density ratio rose from 6.5 before beam injection to 10.0 during the beam pulse. There was little change in the carbon density with beam injection. As shown in Table V, the oxygen density decreased slightly with beam injection; however, in light of the previously discussed uncertainties, the data were also consistent with no change in the oxygen density. The carbon and oxygen concentrations during beam heating were 5% and 0.5%, respectively. Thus, it is clear that carbon was the dominant low-Z impurity both before and during beam injection, and changes in low-Z impurity densities with beam injection were small. As a result of the n_e rise, the central deuteron concentration rose from 54% before beam injection to 66%

during beam injection.

The total radiated power measured by bolometry rose from 780 kW before beam injection to 1900 kW during beam injection, an increase of a factor of 2.4. The total radiated power before beam injection was 50% of the ohmic input power and the total radiated power during beam injection was 30% of the total input power. The total radiated power during beam injection obtained from spectroscopy was 1400 kW, in reasonable agreement with the bolometer measurement. Of this, 195 kW was due to metallic impurities, 367 kW to oxygen, and 838 kW to carbon. Thus, radiative losses both before and during beam heating were primarily due to low-Z impurities, particularly carbon. This is consistent with the observation that the bolometer radiated power profiles were hollow before and during beam heating.

In this context, it is useful to examine the effects of beam-neutral charge-exchange recombination on line brightness calculated by the MIST code and, as a result, on the inferred impurity densities and radiative losses. The code calculations for this discharge were done omitting as well as including beam-neutral charge-exchange recombination. The calculated metallic impurity line brightnesses and radiative losses were the same in both cases. The calculated ratio of the brightness of the CVI 34 Å line to that of the OVIII 19.0 Å line increased by 15% when beam-neutral charge-exchange recombination was omitted; as a result, the carbon-to-oxygen density ratio inferred from the data would change by the same amount. The power radiated by oxygen and carbon decreased by 5%. Similar results were obtained for the other beam-heated discharges discussed in this paper. Thus, the effects of beam-neutral charge-exchange recombination were not an important source of uncertainties in impurity densities and radiative losses for the discharges discussed.

2. Comparison of Ohmic and Neutral Beam Density Scans

Because neutral beam injection is accompanied by an electron density rise, it is important to separate the changes in Z_{eff}, impurity densities, and radiative losses due to beam injection from those caused by the density rise. This is especially important because the mechanism for the density increase, central beam fuelling, is considerably different from gas puffing at

the plasma edge, and thus may result in different impurity production rates. This section compares impurity measurements in $\bar{n}_e$ scans in ohmic- and beam-heated discharges.

Figure 9 shows the variation of Z_{eff} with $\bar{n}_e$ for a series of ohmically-heated discharges at I_p = 2.2 MA and B_T = 4.7 T following chromium gettering. The decrease of Z_{eff} with increasing $\bar{n}_e$ has been observed in ohmic TFTR discharges at lower I_p and B_T [4] and indicates a decrease in the dominant impurity concentration. Also shown in Fig. 9 are values of Z_{eff} from a series of discharges at the same I_p and B_T which had 4-5 MW beam heating. Z_{eff} in these plasmas also decreased with increasing $\bar{n}_e$ and was larger at a given $\bar{n}_e$ than in the ohmic discharges, indicating larger impurity concentrations. To gain more insight into these changes in Z_{eff}, it is instructive to examine the variation with $\bar{n}_e$ of the densities of the major impurity species individually.

Figures 10a and 10b show the central nickel and chromium densities in the ohmic and beam density scans. In both cases, metallic impurity densities decreased with increasing $\bar{n}_e$ [4]. Although there is scatter in the data, metallic impurity densities at high $\bar{n}_e$ were larger by a factor of ~ 2 in the beam-heated discharges than in the ohmic ones. Since a $\bar{n}_e$ rise of the size caused by beam injection would decrease metallic impurity densities, these scalings indicate an increased metallic impurity influx during beam heating. However, the contribution of metallic impurities to the total Z_{eff} continued to be negligible over the entire range of $\bar{n}_e$ in both cases. The decrease in metallic impurity densities with increasing $\bar{n}_e$ was probably due to a decrease in edge electron temperature and, as a result, in sputtering yield [25]. The larger metallic impurity densities at high $\bar{n}_e$ in the beam-heated discharges may be explained by higher edge electron temperatures in these discharges than in ohmic ones, as observed by probe measurements [26]. The limiter temperature also increased with beam injection, from 1200°C with ohmic heating only to 2000°C at 5.6 MW beam power [27]; it is therefore also possible that the increased metallic impurity influx was due to increased evaporation of metal deposited on the limiter.

The carbon-to-oxygen density ratio in these discharges, shown in Fig. 11, decreased with increasing $\bar{n}_e$ in both the ohmic- and beam-heated discharges, and at a given density was somewhat larger in the beam-heated discharges.

Figure 11 shows that carbon was the dominant low-Z impurity at low $\bar{n}_e$: the carbon-to-oxygen density ratio ranged from approximately 10 at low $\bar{n}_e$ to 1-2 at high $\bar{n}_e$. Because metallic impurity densities were small, the impurity contribution to Z_{eff} was due primarily to carbon at low densities and to approximately equal amounts of carbon and oxygen at high densities. The carbon and oxygen densities in these discharges are shown in Figs. 12a and 12b. Like the metallic impurities, the carbon density decreased with increasing $\bar{n}_e$ in both ohmic- and beam-heated discharges. However, the carbon density decreased at a slower rate than the metallic impurity densities. The carbon density in the beam-heated plasmas was larger than in the ohmic ones by a factor of two to three at all electron densities. This behavior is consistent with the lack of a change in the carbon density before and during beam injection in a single discharge: the $\bar{n}_e$ rise with beam injection tended to decrease the carbon density, but the transition from ohmic to neutral beam heating caused an additional influx of carbon. A study of carbon production in TFTR by Ramsey et al. [28] showed that, in addition to sputtering of carbon by deuterons, sputtering by carbon and oxygen were important mechanisms of carbon production. As seen in Fig. 12b, the oxygen density showed a qualitative difference: it rose with increasing $\bar{n}_e$ in both the ohmic- and beam-heated discharges. The primary oxygen source was probably ion and neutral-particle-induced desorption from the walls and limiter. Since desorption yields have a weak energy dependence above the threshold energy [25], the oxygen behavior could be explained by an increase in the particle flux to the walls with increasing $\bar{n}_e$. Within the scatter in the data in Fig. 12b, there was no difference in the oxygen density in the ohmic- and beam-heated plasmas.

Measurements of total power radiated by these plasmas as determined by bolometry and deduced from spectroscopy agree reasonably well, as can be seen in Fig. 13. The radiated power increased gradually with $\bar{n}_e$ in both the ohmic- and beam-heated plasmas and was higher at a given $\bar{n}_e$ in the beam-heated discharges. Metallic impurities contributed 50 kW or less to the total radiated power in the ohmic plasmas and 100 kW or less in the beam-heated discharges; the radiative losses were, therefore, due almost entirely to carbon and oxygen. This may be seen in Fig. 14 where the contribution of each impurity species to the total radiated power in the ohmic $\bar{n}_e$ scan is plotted. The contributions of carbon and oxygen to the total radiated power

varied strongly with $\bar{n}_e$: at $\bar{n}_e$ = 3.6 x 10^{13} cm^{-3} carbon radiated 620 kW and oxygen radiated 260 kW out of a total of 930 kW measured by spectroscopy, and at $\bar{n}_e$ = 5.4 x 10^{13} cm^{-3} carbon radiated 300 kW and oxygen radiated 950 kW out of a total of 1270 kW. Thus, radiated power losses were primarily due to carbon at low densities and to oxygen at high densities. The larger radiated power in the beam-heated discharges than in the ohmic ones was due to increased impurity densities, particularly carbon, and to broader density profiles in the beam-heated discharges. However, radiation was not the dominant mechanism of global energy loss from these plasmas: in the ohmic discharges the fraction of input power radiated ranged from 30% at $\bar{n}_e$ = 3.6 x 10^{13} cm^{-3} to 50% at $\bar{n}_e$ = 5.4 x 10^{13} cm^{-3}; in the beam-heated plasmas the radiated power fraction did not vary within the scatter of the data and was 25-35% for all discharges in the density scan.

Given that the major impurities were low-Z and hence, radiative losses in the core plasma were negligible, the major effect of impurities on core plasma condition was dilution of the plasma working gas at fixed electron density. Such dilution can be detrimental to the plasma reactivity. Figure 15 shows the deuteron concentration on axis in the ohmic- and beam-heated density scans. In ohmically-heated plasmas the deuteron concentraton changed from 70% at $\bar{n}_e$ = 3.6 x $10^{13}cm^{-3}$ to 85% at $\bar{n}_e$ = 5.5 x $10^{13}cm^{-3}$; in beam-heated discharges the deuteron concentration rose from 50% to 80% over the same density range. For both ohmic- and beam-heated plasmas, the deuteron dilution was greatest at low $\bar{n}_e$. Because Z_{eff} was higher at a given $\bar{n}_e$ in the beam-heated discharges than in the ohmic ones, the deuteron concentration was lower in the beam-heated discharges. Although the dilution decreased with $\bar{n}_e$, the net reactivity of the plasma was still reduced by aproximately 40%, all else being equal, at the highest densities achieved.

3. Variations with Neutral Beam Power

This section presents impurity measurements before and during beam heating in a series of discharges with I_p = 2.2 MA, B_T = 4.7 T, and beam power ranging from zero to 5.6 MW. (The discharge discussed in section IV.1 was part of this scan.) In these discharges the beam pulse lasted from 2.8 sec to 3.3 sec; measurements before beam injection were made at 2.75 sec and those during beam injection at 3.25 sec. The $\bar{n}_e$ at the end of the beam pulse was held constant at ~4.6 x 10^{13} cm^{-3} for all discharges in the scan by adjusting

the pre-injection $\bar{n}_e$. Because the density rise with beam injection was larger at higher beam power, $\bar{n}_e$ before beam injection was lower in the higher beam power discharges. The pre-injection $\bar{n}_e$ in the discharges with beam injection ranged from 4.2×10^{13} cm^{-3} at 1.2 MW beam power to 3.1×10^{13} cm^{-3} at 5.6 MW. A discharge with ohmic heating only was also included in the scan.

Figure 16 shows Z_{eff} before and during beam injection in these discharges. Z_{eff} before beam injection ranged from 2.0 to 3.6 and was larger in the discharges with higher beam power due to their lower pre-injection $\bar{n}_e$. As previously discussed, the Z_{eff} drop with beam injection was primarily due to the $\bar{n}_e$ rise. Z_{eff} during the beam pulse rose from 2.0 to 2.8 as the beam power increased from zero to 5.6 MW: because $\bar{n}_e$ was constant, the average impurity density increased with beam power.

Central nickel and chromium densities before and during beam heating are shown in Figs. 17a and 17b. Again, metallic impurity concentrations were small in all of these discharges, less than 0.01% of $n_e(0)$. Metallic impurity densities were larger during beam injection than before it, and increased with beam power. Because the pre-injection $\bar{n}_e$ was lower in the higher beam power discharges, metallic impurity densities before beam injection were somewhat higher in the higher power discharges.

Figure 18 shows the carbon-to-oxygen density ratio before and during beam injection. Carbon was the major impurity contributor to Z_{eff}, both before and during beam injection, in almost all of these discharges. The carbon-to-oxygen density ratio before beam injection was larger in the plasmas with greater beam power; because the pre-injection $\bar{n}_e$ decreased with beam power, this is consistent with the $\bar{n}_e$ scaling of the previous section. With one exception, the carbon-to-oxygen density ratio in a given discharge was larger during beam injection than before it; the difference was always a factor of two or less, and did not vary systematically with beam power. The carbon-to-oxygen density ratio during beam injection increased with beam power.

Figures 19a and 19b show the central carbon and oxygen densities before and during beam injection. During a particular discharge, the central carbon density was not different before and during beam injection. The pre-injection carbon density was larger in the lower initial density, higher beam power discharges, consistent with the $\bar{n}_e$ scaling discussed in the previous section. The carbon density during beam heating increased with beam power.

The pre-injection oxygen density shown in Fig. 19b was not significantly different for discharges at different beam power levels and hence different pre-injection electron densities. This is consistent with the oxygen density scaling with $\bar{n}_e$ over the range 3.1×10^{13} cm^{-3} to 4.2×10^{13} cm^{-3} shown in Fig. 12b. Fig. 19b also shows that the oxygen density during beam injection did not change significantly with beam power. In a given discharge, the measured oxygen density during beam injection was lower in almost all cases than the measured oxygen density before injection. The explanation for this behavior is not clear.

Figure 20 shows the total power radiated during neutral beam injection as measured by bolometry and spectroscopy. As in the $\bar{n}_e$ scans, the two measurements are in reasonable agreement. The total radiated power measured by bolometry increased with beam power from 1120 kW with ohmic heating only to 1950 kW at 5.6 MW beam power. The total radiated power before beam injection measured by bolometry did not vary significantly and was in the 750-1120 kW range. Also shown in Fig. 20 is the power radiated by nickel and chromium, which rose from 90 kW with ohmic heating only to 200 kW at 5.6 MW beam power; thus metallic impurity radiation was a small part of the total radiated power. As shown in Fig. 20, the power radiated by carbon was larger than that radiated by oxygen for all discharges in the scan. Thus, the radiated power increase with beam power was due primarily to the increase in carbon density with beam power. Because this increase in radiated power was less rapid than the increase in input power, the fraction of input power radiated decreased from 50% with ohmic heating to 30% at beam powers greater than 3 MW. (The ohmic heating power dropped from 2.0 MW with ohmic heating only to 1.3 MW at 5.6 MW beam power.)

The deuteron concentration in these plasmas is shown in Fig. 21. As a result of lower pre-injection Z_{eff}, the deuteron concentration before beam injection was larger in the lower beam power plasmas, in agreement with the deuteron concentration scaling with $\bar{n}_e$ shown in Fig. 14. In a single discharge the deuteron concentration was larger during beam injection than before injection as a result of the Z_{eff} drop with beam injection. The deuteron concentration during beam injection decreased with beam power from 85% of $n_e(0)$ with ohmic heating to 65% with 5.6 MW beam power.

V. Summary

Measurements of extreme UV line intensities and of the visible continuum coupled with an impurity transport code allow quantitative spectroscopic measurements of impurity behavior in individual discharges. While uncertainties in such measurements have a number of causes, especially in the case of low-Z impurities in high temperature plasmas, reasonably simple transport models and careful evaluation of the sensitivity of the results to model assumptions allow detailed measurements of Z_{eff}, impurity densities, and radiative losses.

An in-depth documentation of impurity behavior in ohmic- and beam-heated discharges (L-Mode energy confinement) with I_p = 2.2 MA, B_T = 4.7 T, and beam power up to 5.6 MW revealed several general trends. Z_{eff} during beam injection dropped from the pre-injection level due to an increase in plasma density by beam fuelling, while the density of the dominant impurity species, carbon, did not increase significantly. Although metallic impurity densities rose somewhat during beam injection, their concentrations and radiative losses from them were negligible. The densities of carbon and the metals dropped with increasing $\bar{n}_e$, while the oxygen density increased. As a result, radiated power losses in ohmic plasmas were primarily due to carbon at low $\bar{n}_e$ and to oxygen at high $\bar{n}_e$. With beam heating, carbon tended to dominate the radiative losses. While carbon and metal densities increased with beam power, the oxygen density showed little variation. Since metallic impurity concentrations were negligible, the radiated power profiles were hollow in all cases. The total radiated power ranged from 50% with ohmic heating to 30% for beam power levels of 3-5.6 MW. Finally, both quantitative line intensity modelling and radially resolved Z_{eff} measurements showed no evidence of central impurity accumulation in TFTR plasmas with ohmic heating or co-tangential beam injection.

In light of these results, it appears that the primary role of impurities in these discharges with moderate beam power was the modification of edge plasma conditions due to peripheral radiation from low-Z impurities and, in the plasma core, reduction of the plasma reactivity through fuel dilution. Although the former effect may be beneficial in providing a cool plasma edge, the latter effect is potentially detrimental. At 5.6 MW beam power, the central deuteron concentration was already down to 70% of $n_e(0)$, resulting in

a factor of two loss in potential plasma neutron production. Also, the slow rise in Z_{eff} seen with increasing beam power points to increasing plasma dilution at higher beam power levels. Diagnosis and control of low-Z impurity production in TFTR will, therefore, continue to be a subject of considerable importance.

ACKNOWLEDGMENTS

We would like to thank K.M. Young and the entire TFTR group for their support of this work. Particular thanks are due to B. Grek, D. Johnson, B. LeBlanc, D. McNeill, H. Park, F. Stauffer, and G. Taylor for providing electron temperature and density measurements, D. Heifetz for neutral density calculations, K. Hill and S. Sesnic for comparisons with soft x-ray pulse-height-analysis results, and H.F. Dylla for useful discussions. This work was supported by U.S. DoE Contract No. DE-AC02-76-CHO-3073.

REFERENCES

[1] ISLER, R.C., Nucl. Fusion 24 (1984) 1599.

[2] KEILHACKER, M., FUSSMANN, G., VON GIERKE, G., JANESCHITZ, G., KORNHERR, M., et al., in Plasma Physics and Controlled Nuclear Fusion Research (Proc. 10th Intl. Conf., London, 1984) IAEA, Vienna (1985) Vol. I, p. 71.

[3] IDA, K., FONCK, R.J., SESNIC, S., HULSE, R.A., LEBLANC, B., Princeton Plasma Physics Laboratory Report PPPL-2313 (1986).

[4] HILL, K.W., BITTER, M., BRETZ, N.L., EFTHIMION, P.C., DIESSO, M., et al., Nucl. Fusion 26 (1986) 1131.

[5] MURAKAMI, M., ARUNASALAM, V., BELL, J.D., BELL, M.G., BITTER, M., et al., Fusion Technol. 8 (1985) 657.

[6] MURAKAMI, M., ARUNASALAM, V., BELL, J.D., BELL, M.G., BITTER, M., et al., Plasma Phys. Controlled Fusion 28 (1986) 17.

[7] DYLLA, H.F., BELL, M.G., BLANCHARD, W.R., BOODY, F.P., BRETZ, N.L., et al., Presented at Plasma-Surface Interactions Conference, Princeton, May 1986. To be published in J. Nucl. Mater., Princeton Plasma Physics Laboratory Report, PPPL-2386, October 1986.

[8] LAMARCHE, P.H., DYLLA, H.F., BELL, M.G., BOODY, F.P., et al., Presented at Plasma-Surface Interactions Conference, Princeton, May 1986. To be published in J. Nucl. Mater.

[9] FONCK, R.J., RAMSEY, A.T., YELLE, R.V., Appl. Opt. 21 (1982) 2115.

[10] STRATTON, B.C., FONCK, R.J., IDA, K., JAEHNIG, K.P., RAMSEY, A.T., Rev. Sci. Instrum., 57 (1986) 2043.

[11] SCHWOB, J.L., FINKENTHAL, M., SUCKEWER, S., in Vacuum Ultraviolet Radiation Physics, VUV VII, (Proceedings of the 7th International Conference, Jerusalem, 1983).

[12] HEIFETZ, D.B., in Physics of Plasma-Wall Interactions in Controlled Fusion, edited by D.E. Post and R. Behrisch, Plenum, New York (1986).

[13] FONCK, R.J., DARROW, D.S., JAEHNIG, K.P., Phys. Rev. A. 26, (1984) 3288.

[14] RAMSEY, A.T., TURNER, S.L., submitted to Rev. Sci. Instrum. 1986.

[15] SESNIC, S., and HILL, K.W., Private Communication.

[16] HULSE, R.A., Nucl. Technol./Fusion 3 (1983) 259.

[17] TOWNER, H.H., BELL, M.G., COONROD, J., DAVIS, S.L., et al., Bull. Am. Phys. Soc. 28 (1983) 1252.

[18] STRATTON, B.C., COHEN. S.A. BOODY, F.P., BUSH, C.E., et al., Presented at Plasma-Surface Interactions Conference, Princeton, May, 1986. To be published in J. Nucl. Mater., Princeton Plasma Physics Laboratory Report, PPPL-2393, October 1986.

[19] HULSE, R.A., in Princeton Plasma Physics Laboratory Report PPPL-2182, edited by C.E. Singer (1985).

[20] KILPATRICK, S.J., MANOS, D.M., BUDNY, R.V., STANGEBY., P.C., et al., J. Vac. Sci. Technol. A, 4 (1986) 1817.

[21] MEWE, R., Astron. Astrophys. 20 (1972) 215.

[22] POST, D.E., JENSEN, R.V. TARTER, C.B., GRASBERGER, W.H., LOKKE, W.A., At. Data Nucl. Data Tables 20 (1977) 397.

[23] FELDMAN, U., SEELY, J.F., BHATIA, A.K., At. Data Nucl. Data Tables 32 (1985) 305.

[24] HAWRYLUK, R.J., SUCKEWER, S., HIRSHMAN, S.P., Nucl. Fusion 19 (1979) 607.

[25] MCCRACKEN, G.M., STOTT, P.E., Nucl. Fusion 19 (1979) 889.

[26] MANOS, D.M, Private Communication.

[27] ULRICKSON, M., J. Vac. Sci. Technol. A, 4 (1986) 1805.

[28] RAMSEY, A.T., STRATTON, B.C, BOODY, F.P., BUSH, C.E., et al., presented at the Plasma-Surface Interactions Conference, Princeton, May 1986. To be published in J. Nucl. Mater.

TABLE I.

Metallic Impurity Analysis for Example Discharge

Ion	λ(Å)	Measured Brightness*	Calculated Brightness*	Brightness Ratio
NiXVII	249	2.8	3.2	0.88
NiXVIII	292	2.3	3.1	0.74
NiXVIII	321	1.5	1.7	0.88
NiXXV	118	2.5	2.8	0.89
NiXXVI	165	3.6	2.8	1.29
NiXXVI	234	1.9	1.4	1.36
CrXIII	328	0.75	1.1	0.68
CrXIV	389	1.1	1.1	1.00
CrXIV	412	0.51	0.58	0.88
CrXXII	223	2.7	2.4	1.13
CrXXII	280	1.4	1.2	1.17

* (10^{13} photons/sec-cm^2-sr)

TABLE II.

PLASMA COMPOSITION IN EXAMPLE DISCHARGE

Element	Central Density	Central Concentration	Z_{eff}	$P_{rad}(0)$	Total P_{rad}
C	1.9×10^{12} cm^{-3}	0.042	1.48	4.7 mW/cm^3	416 kW
O	1.9×10^{11}	0.0041	0.26	1.2	180
Ni	1.1×10^{9}	2.4×10^{-5}	0.014	0.5	30
Cr	9.0×10^{8}	2.0×10^{-5}	0.009	0.2	14
D	3.3×10^{13}	0.72	0.72	1.1	---
Total			**2.48**	**7.7**	**640**
Measured			**2.50**	**9**	**705**

TABLE III

Calculated Carbon and Oxygen Line Brightnesses

	REFERENCE CASE	D(X2)	D(÷2)	C_V(X2)	C_V(÷2)	RECOMB. RATES (X2)	RECOMB. RATES (÷2)	ION. RATES (X2)	ION. RATES (÷2)	n_e(X2)	n_e(÷2)	T_e(X2)	T_e(÷2)	IMPURITY SOURCE RADIUS = 82 cm	IMPURITY SOURCE RADIUS = 90 cm	S.O.L. PARALLEL LOSS λ (X2)	S.O.L. PARALLEL LOSS λ (÷2)	S.O.L. T_e λ(X2)	S.O.L. T_e λ(÷2)	S.O.L. n_e λ(X2)	S.O.L. n_e λ(÷2)	IMPURITY SOURCE ENERGY (X10)	IMPURITY SOURCE ENERGY (÷10)	THERMAL NEUTRAL DENSITY (X2)	THERMAL NEUTRAL DENSITY (÷2)
CVI 34A	1.2	1.5	0.96	0.57	1.8	1.4	1.0	0.72	1.9	3.2	0.45	0.91	1.7	1.2	1.2	1.1	1.3	1.2	1.2	1.2	1.1	1.1	1.2	1.5	1.0
OVIII 19A	1.7	1.9	1.4	0.97	2.1	2.2	1.3	0.95	2.8	5.0	0.56	1.1	2.7	1.6	1.7	1.6	1.7	1.6	1.6	1.6	1.6	1.6	1.6	2.0	1.4
$\frac{\text{CVI 34A}}{\text{OVIII 19A}}$	0.71	0.79	0.69	0.59	0.86	0.64	0.77	0.76	0.68	0.64	0.80	0.83	0.63	0.75	0.71	0.69	0.76	0.75	0.75	0.75	0.69	0.69	0.75	0.75	0.71
CIV 384A	0.37	0.72	0.19	0.08	0.79	0.38	0.37	0.19	0.74	0.89	0.15	0.24	0.64	0.37	1.2	0.24	0.63	0.36	0.41	0.46	0.26	0.25	0.47	0.38	0.37
OVI 173A	1.2	1.5	0.85	0.25	2.5	1.2	1.2	0.82	1.6	4.1	0.32	0.95	1.2	0.63	1.2	0.74	1.8	1.2	0.88	2.4	0.48	0.70	1.4	1.2	1.1
$\frac{\text{CIV 384A}}{\text{OVI 173A}}$	0.31	0.48	0.22	0.34	0.32	0.32	0.31	0.23	0.46	0.22	0.47	0.25	0.53	0.59	1.00	0.32	0.35	0.30	0.30	0.20	0.54	0.36	0.34	0.32	0.34

Brightness units: 10^{13} photons/sec-cm^2-sr

TABLE IV

Low-Z Impurity Analysis

	Ion	λ(Å)	Measured Brightness*	Calculated Brightness†*	Brightness Ratio
	CIV	384	2.1	0.37	5.7
LiI-like Ions	CIV	420	1.1	0.18	6.1
	OVI	173	0.81	1.2	0.68
	OVI	184	0.45	0.65	0.69
HI-like Ions	CVI	34	18.0	1.1	16.4
	OVIII	19	2.4	1.5	1.6

* (10^{13} photons/sec-cm^2-sr)

† assumes 0.1% carbon and oxygen concentrations

TABLE V

Central Impurity Densities Before and During Beam Heating at 5.6 MW

Element	Density Before Beam Heating	Density During Beam Heating
C	$2.8 \times 10^{12} cm^{-3}$	$2.9 \times 10^{12} cm^{-3}$
O	4.3×10^{11}	2.9×10^{11}
Ni	2.2×10^{9}	4.7×10^{9}
Cr	8.0×10^{8}	2.2×10^{9}

FIGURE CAPTIONS

FIG. 1. SPRED spectrum of 100-1100 Å region from example discharge (I_p = 2.2 MA, B_T = 4.7 T, $\bar{n}_e$ = 3.6 x $10^{13}cm^{-3}$) integrated for 0.1 sec. The instrumental sensitivity decreases with increasing wavelength by two orders of magnitude over the region shown here.

FIG. 2. SOXMOS spectrum of 15-36 Å region from example discharge integrated for 0.1 sec.

FIG. 3. Measured T_e and n_e profiles at 3.35 sec in example discharge.

FIG. 4. Calculated nickel ion radial distribution for example discharge. (For clarity only the higher ionization states are shown.)

FIG. 5. Spectroscopic and bolometric radiated power profiles for example discharge.

FIG. 6. Time evolution of $\bar{n}_e$ in a beam-heated discharge with 5.6 MW beam power, I_p = 2.2 MA and B_T = 4.7 T.

FIG. 7. Z_{eff} profiles from discharges with 5.6 MW beam power and ohmic heating only at I_p = 2.2 MA, B_T = 4.7 T, and $\bar{n}_e$ = 4.6 x $10^{13}cm^{-3}$.

FIG. 8. Time evolution of impurity line brightnesses in a discharge with 5.6 MW beam power.

FIG. 9. Z_{eff} scaling with $\bar{n}_e$ in beam (4-5 MW) and ohmically heated discharges with I_p = 2.2 MA and B_T = 4.7 T.

FIG. 10. Central nickel (a) and chromium (b) densities in beam and ohmically heated $\bar{n}_e$ scans.

FIG. 11. Carbon density to oxygen density ratio in beam and ohmically heated $\bar{n}_e$ scans.

FIG. 12. Central carbon (a) and oxygen (b) densities in beam and ohmically heated $\bar{n}_e$ scans.

FIG. 13. Total radiated power measured by bolometry and spectroscopy in beam-heated and ohmic $\bar{n}_e$ scans.

FIG. 14. Power radiated by each impurity element in ohmic $\bar{n}_e$ scan.

FIG. 15. Deuteron concentration for beam and ohmically heated $\bar{n}_e$ scans.

FIG. 16 Z_{eff} before and during beam heating in beam power scan at I_p = 2.2 MA and B_T = 4.7 T.

FIG. 17. Central nickel (a) and chromium (b) densities before and during beam heating in beam power scan.

FIG. 18. Carbon density to oxygen density ratio before and during beam heating in beam power scan.

FIG. 19. Central carbon (a) and oxygen (b) densities before and during beam heating in beam power scan.

FIG. 20. Total radiated power measured by bolometry and spectroscopy and power radiated by metallic impurities, carbon, and oxygen during beam heating in beam power scan.

FIG. 21. Deuteron concentration before and during beam heating in beam power scan.

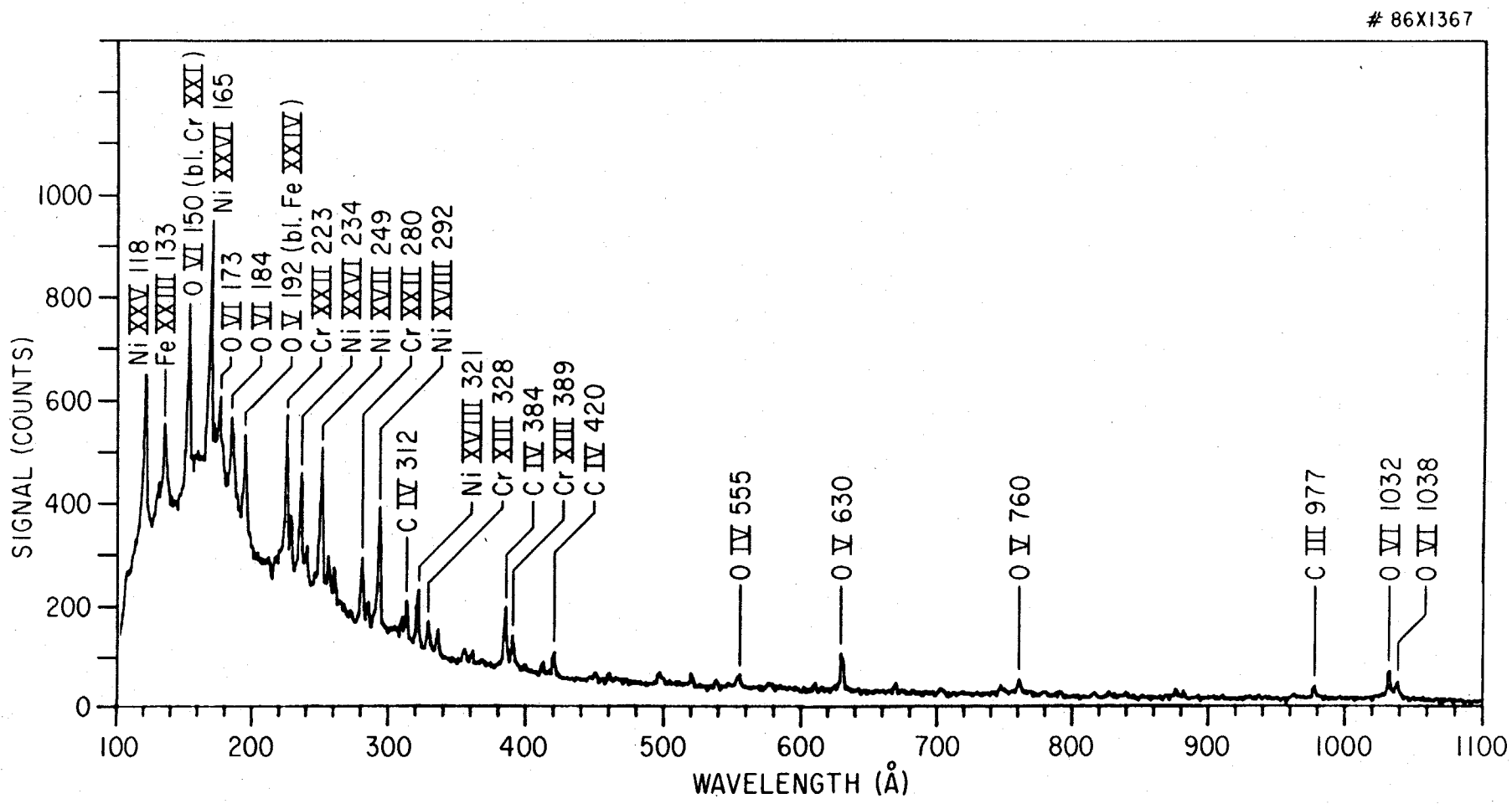
86X1367
SIGNAL (COUNTS)
WAVELENGTH (Å)
Ni XXV 118
Fe XXIII 133
O VII 150 (bl. Cr XXI)
Ni XXVI 165
O VII 173
O VII 184
O V 192 (bl. Fe XXIV)
Cr XXII 223
Ni XXVI 234
Ni XVII 249
Cr XXII 280
Ni XVIII 292
C IV 312
Ni XVIII 321
Cr XIII 328
C IV 384
Cr XIII 389
C IV 420
O IV 555
O V 630
O V 760
C III 977
O VI 1032
O VI 1038

Fig. 1

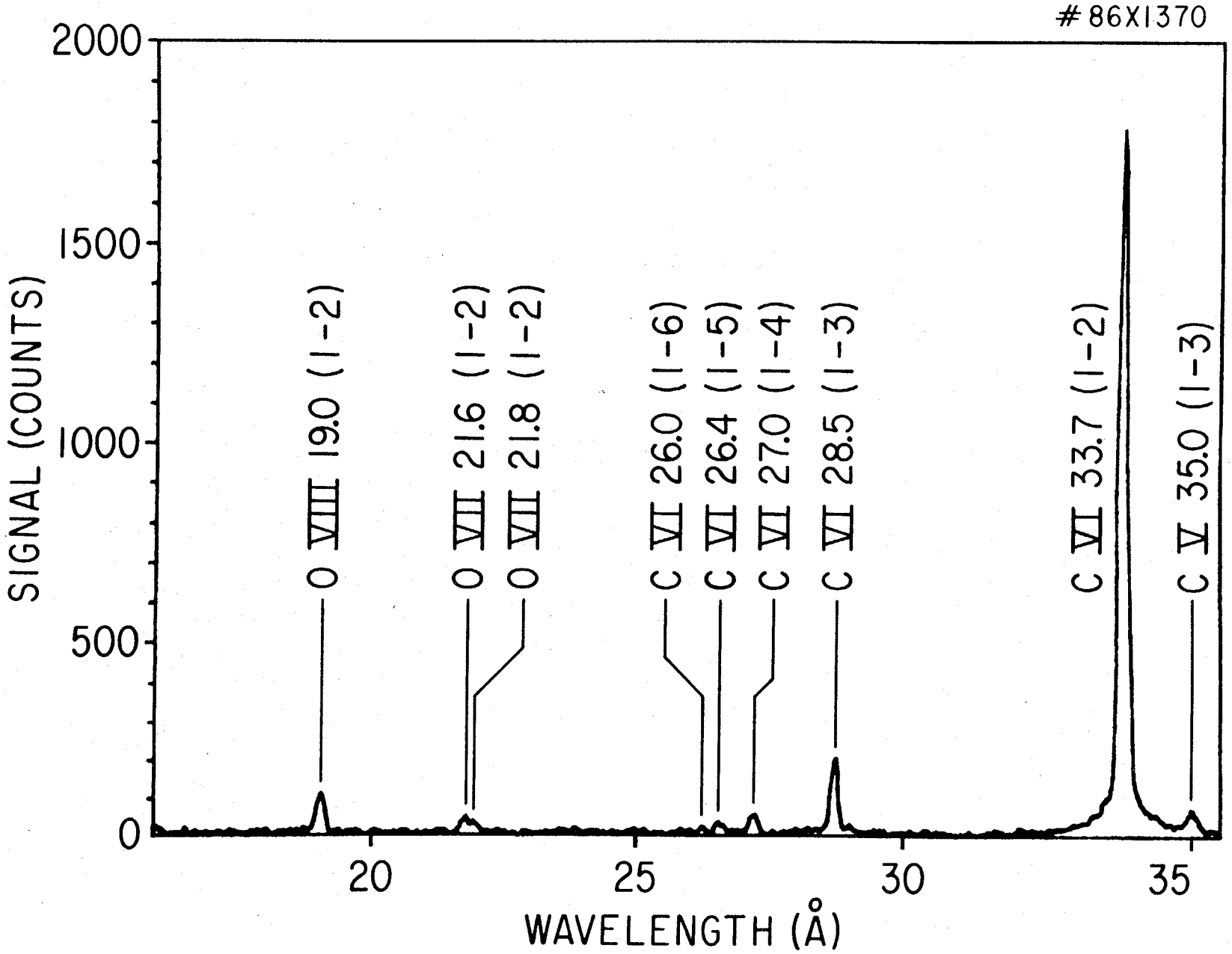
#86X1370
2000
1500
1000
500
0
SIGNAL (COUNTS)
O VIII 19.0 (1-2)
O VII 21.6 (1-2)
O VII 21.8 (1-2)
C VI 26.0 (1-6)
C VI 26.4 (1-5)
C VI 27.0 (1-4)
C VI 28.5 (1-3)
C VI 33.7 (1-2)
C V 35.0 (1-3)
20
25
30
35
WAVELENGTH (Å)

Fig. 2

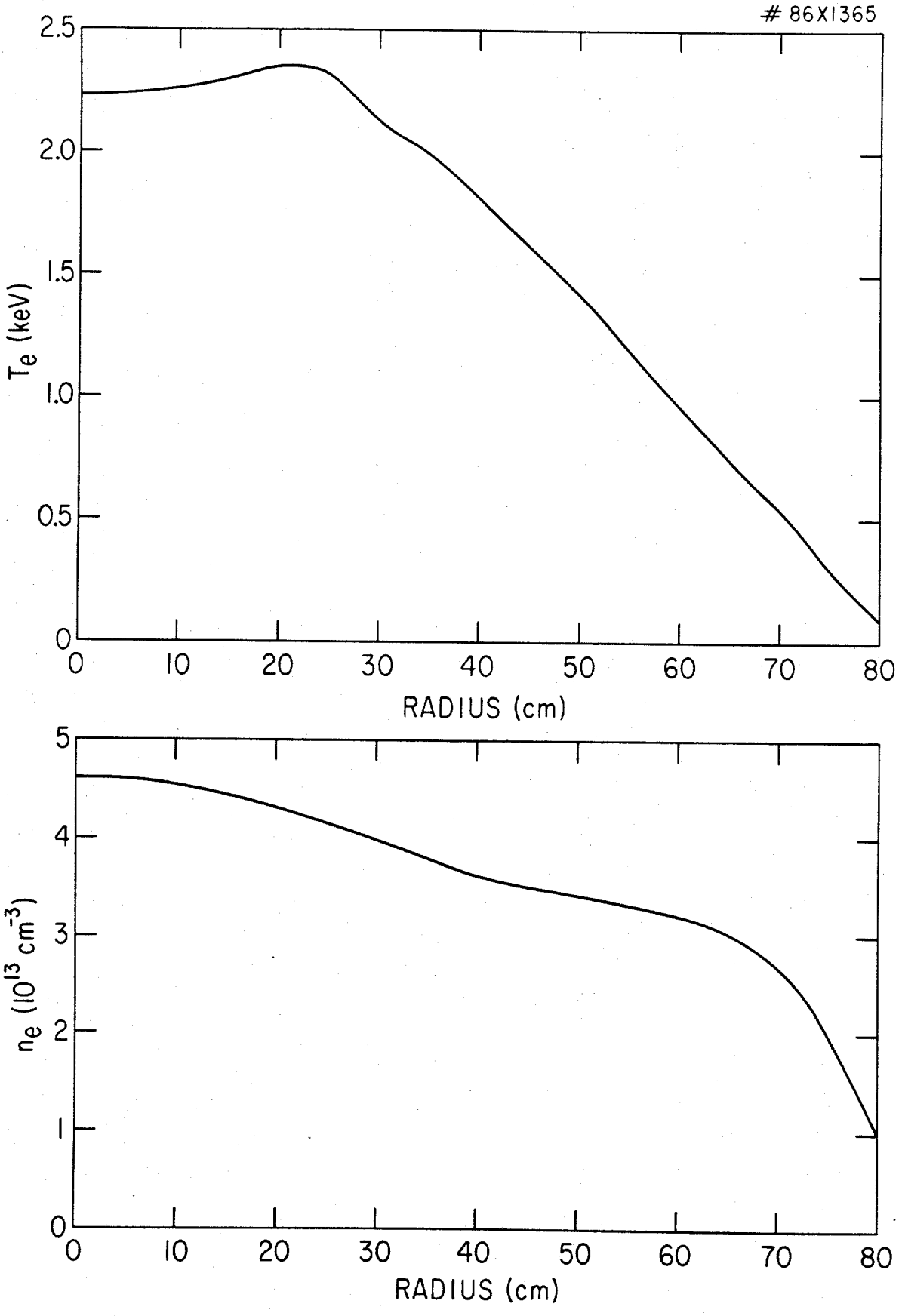
86X1365
2.5
2.0
1.5
1.0
0.5
0
T_e (keV)
0
10
20
30
40
50
60
70
80
RADIUS (cm)
5
4
3
2
1
0
n_e (10^{13} cm^{-3})
0
10
20
30
40
50
60
70
80
RADIUS (cm)

Fig. 3

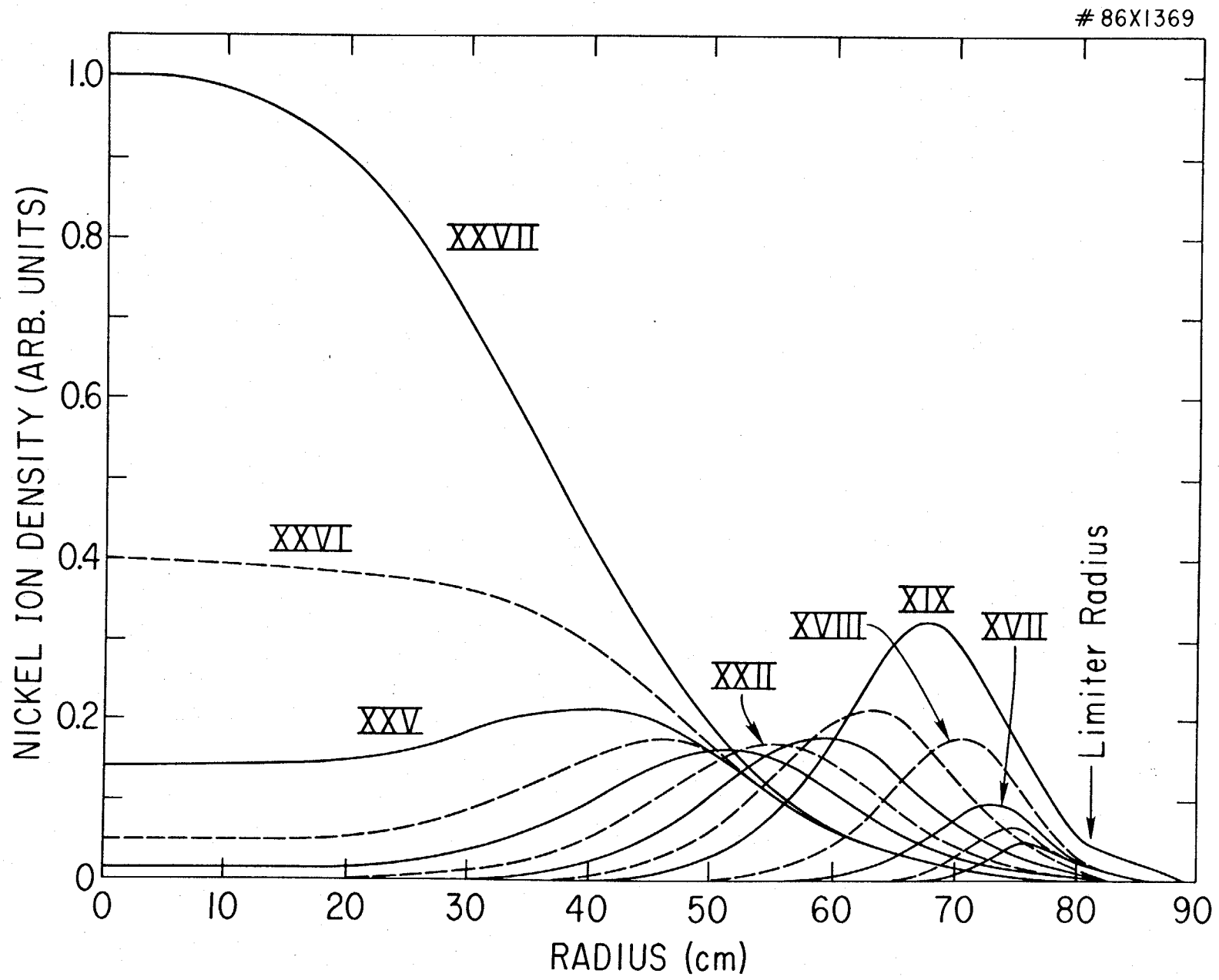
#86X1369
NICKEL ION DENSITY (ARB. UNITS)
1.0
0.8
0.6
0.4
0.2
0
0
10
20
30
40
50
60
70
80
90
RADIUS (cm)
XXVII
XXVI
XXV
XXII
XVIII
XIX
XVII
Limiter Radius

Fig. 4

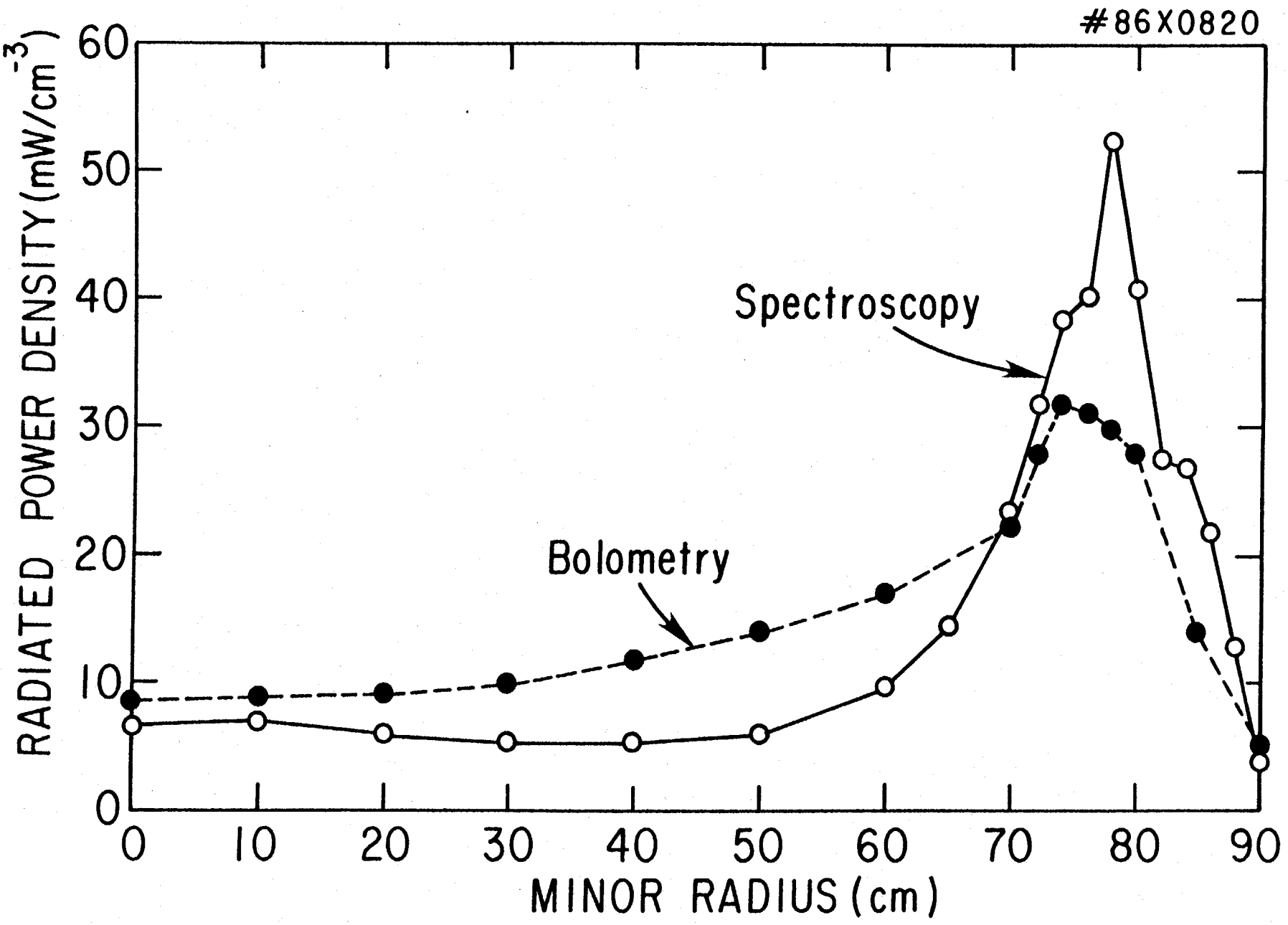
#86X0820
RADIATED POWER DENSITY (mW/cm^{-3})
0
10
20
30
40
50
60
Spectroscopy
Bolometry
0
10
20
30
40
50
60
70
80
90
MINOR RADIUS (cm)

Fig. 5

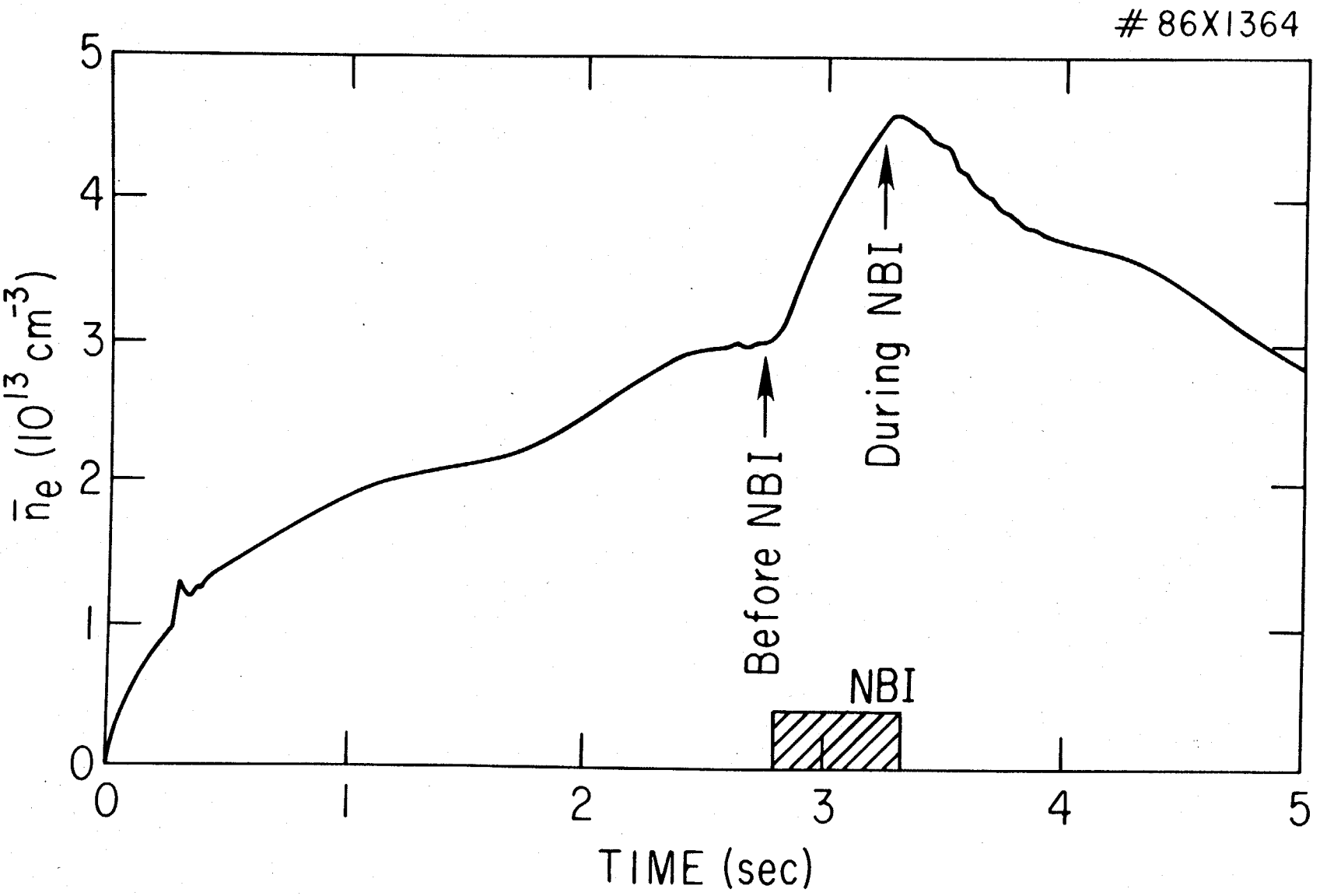
#86X1364
$\bar{n}_e$ (10^{13} cm^{-3})
TIME (sec)
Before NBI
During NBI
NBI
0
1
2
3
4
5

Fig. 6

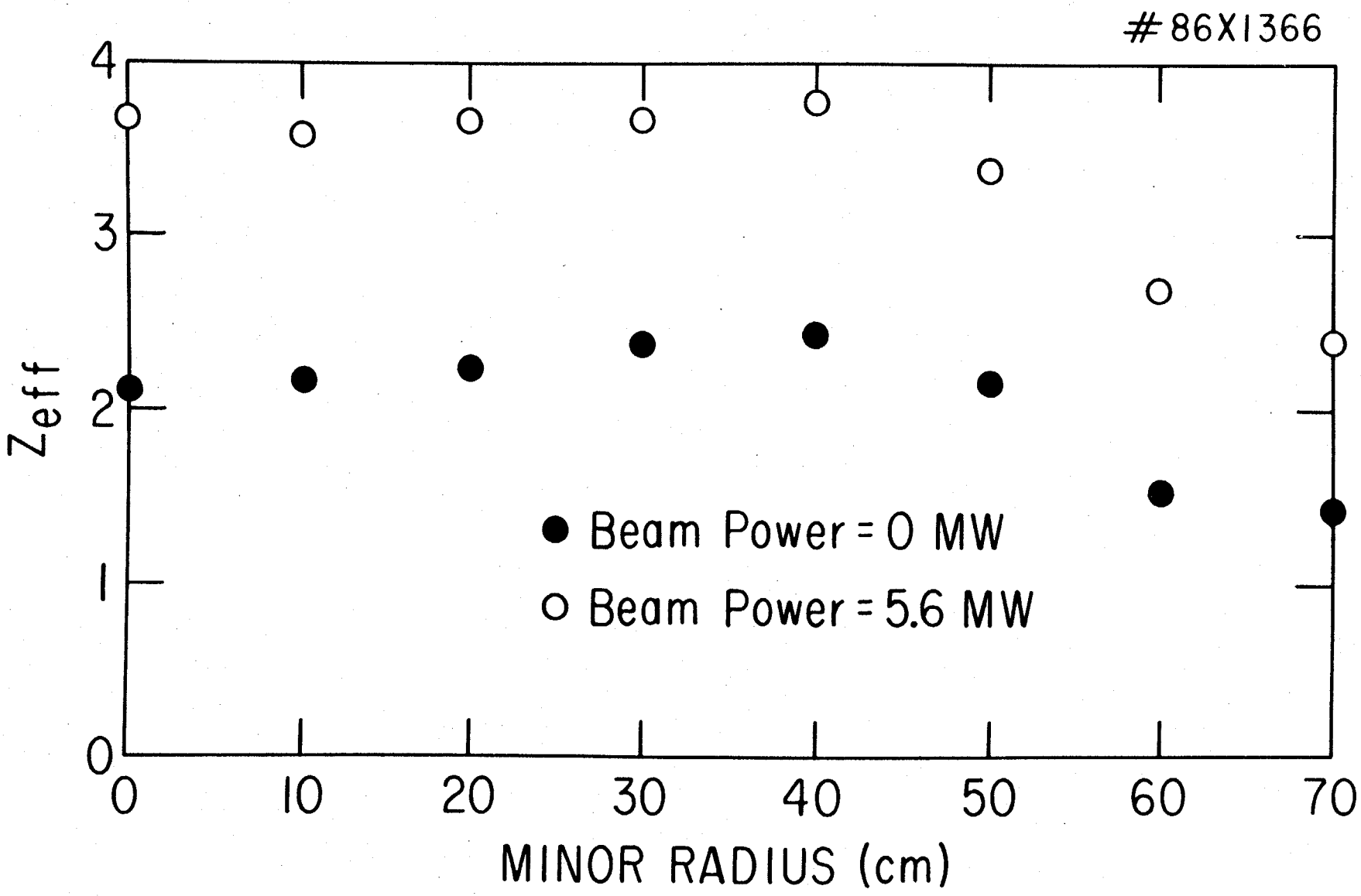
#86X1366
4
3
2
1
0
Z_{eff}
● Beam Power = 0 MW
○ Beam Power = 5.6 MW
0
10
20
30
40
50
60
70
MINOR RADIUS (cm)

Fig. 7

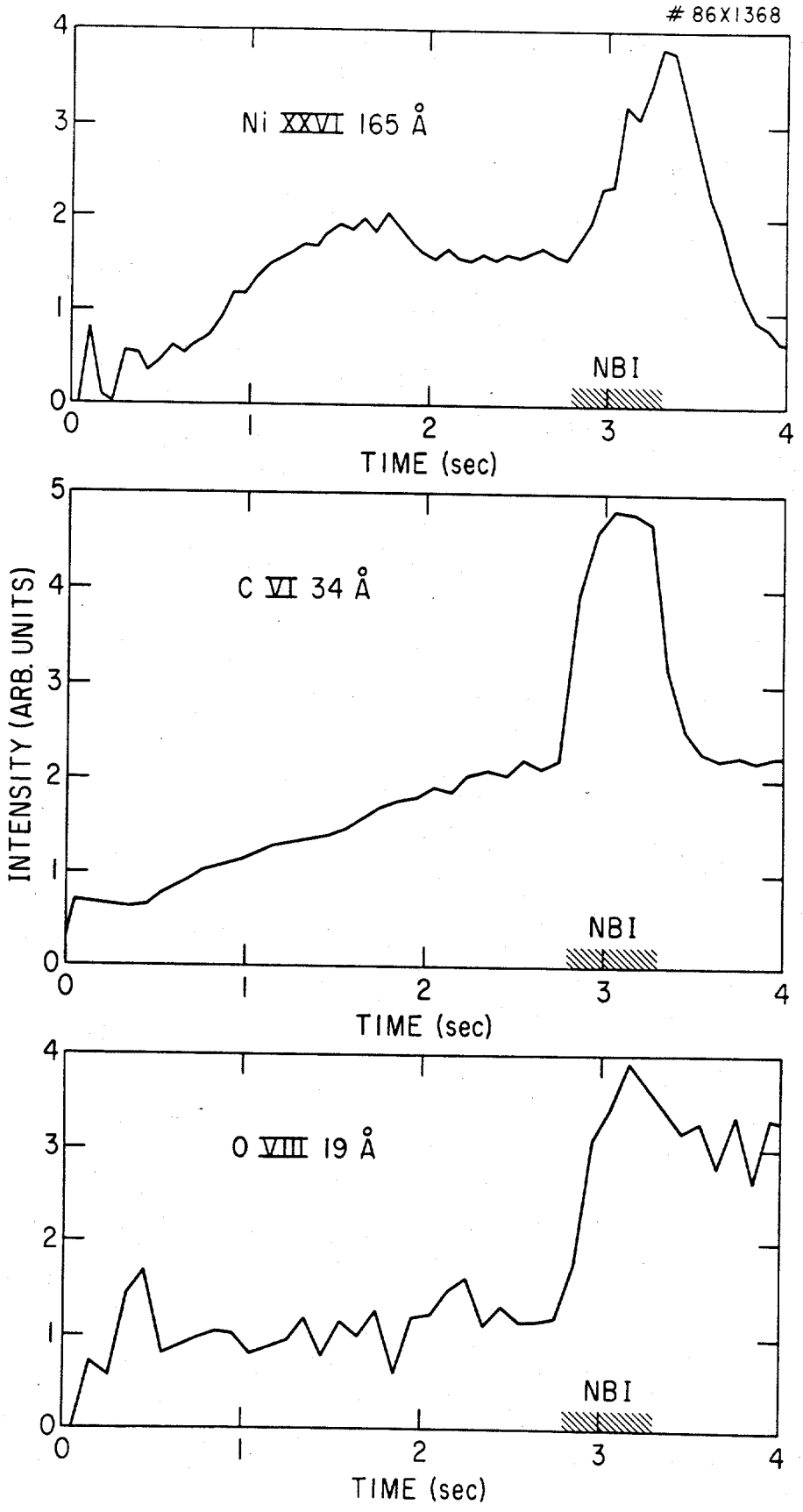
86X1368
Ni XXVI 165 Å
NBI
TIME (sec)
C VI 34 Å
NBI
INTENSITY (ARB. UNITS)
TIME (sec)
O VIII 19 Å
NBI
TIME (sec)

Fig. 8

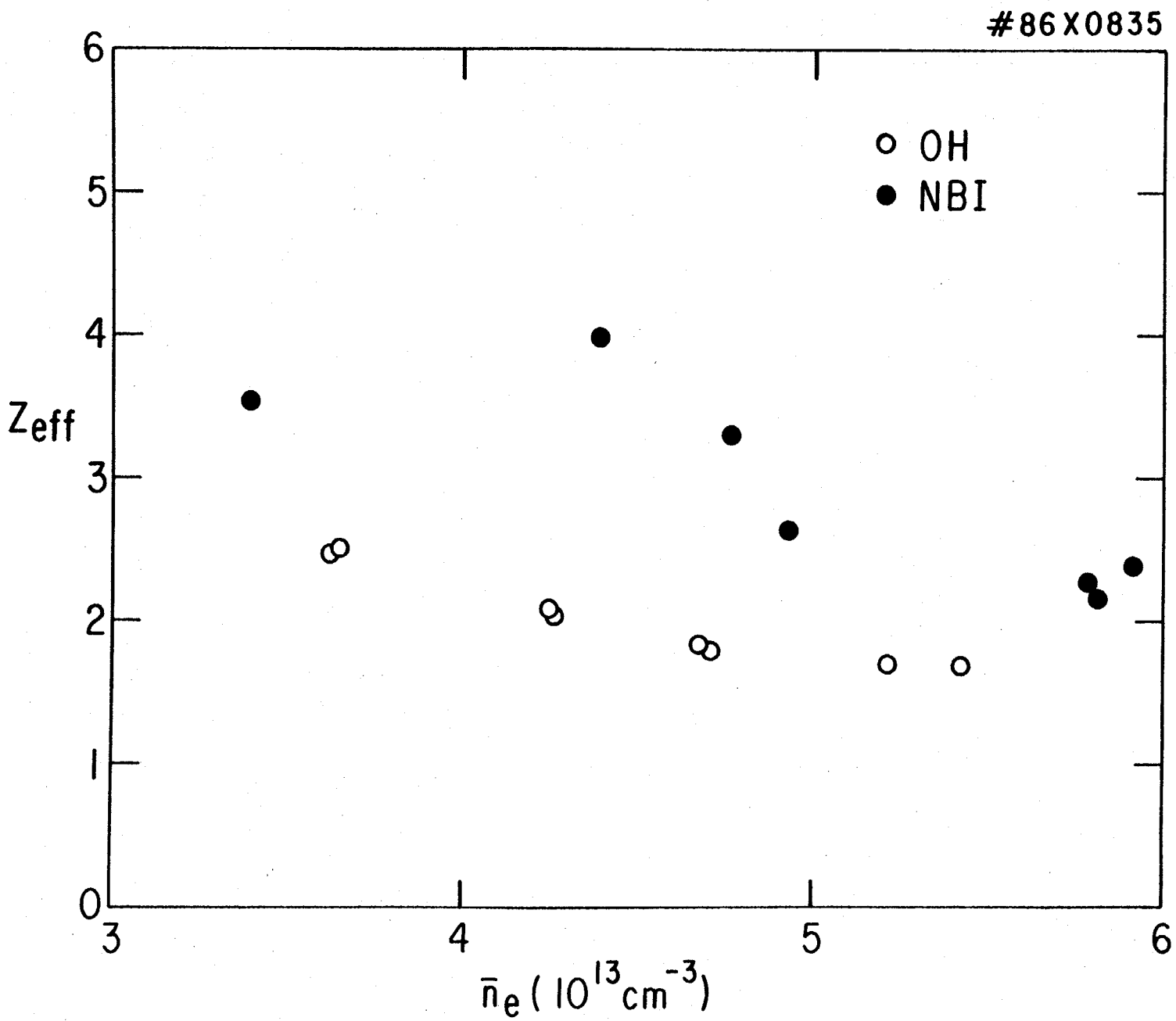

Fig. 9

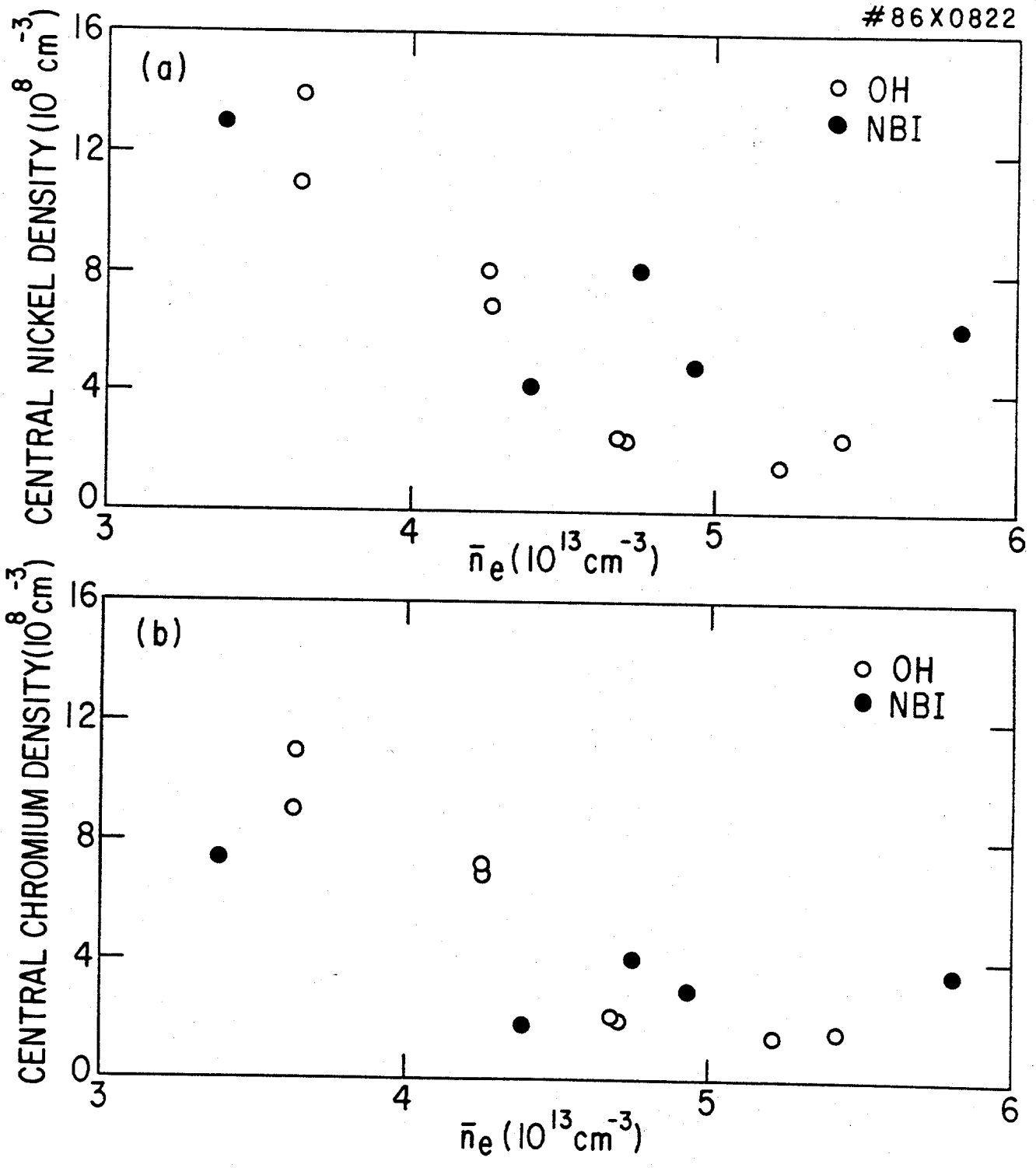
#86X0822
(a)
CENTRAL NICKEL DENSITY (10^8 cm^{-3})
OH
NBI
$\bar{n}_e$ (10^{13} cm^{-3})
(b)
CENTRAL CHROMIUM DENSITY (10^8 cm^{-3})
OH
NBI
$\bar{n}_e$ (10^{13} cm^{-3})

Fig. 10

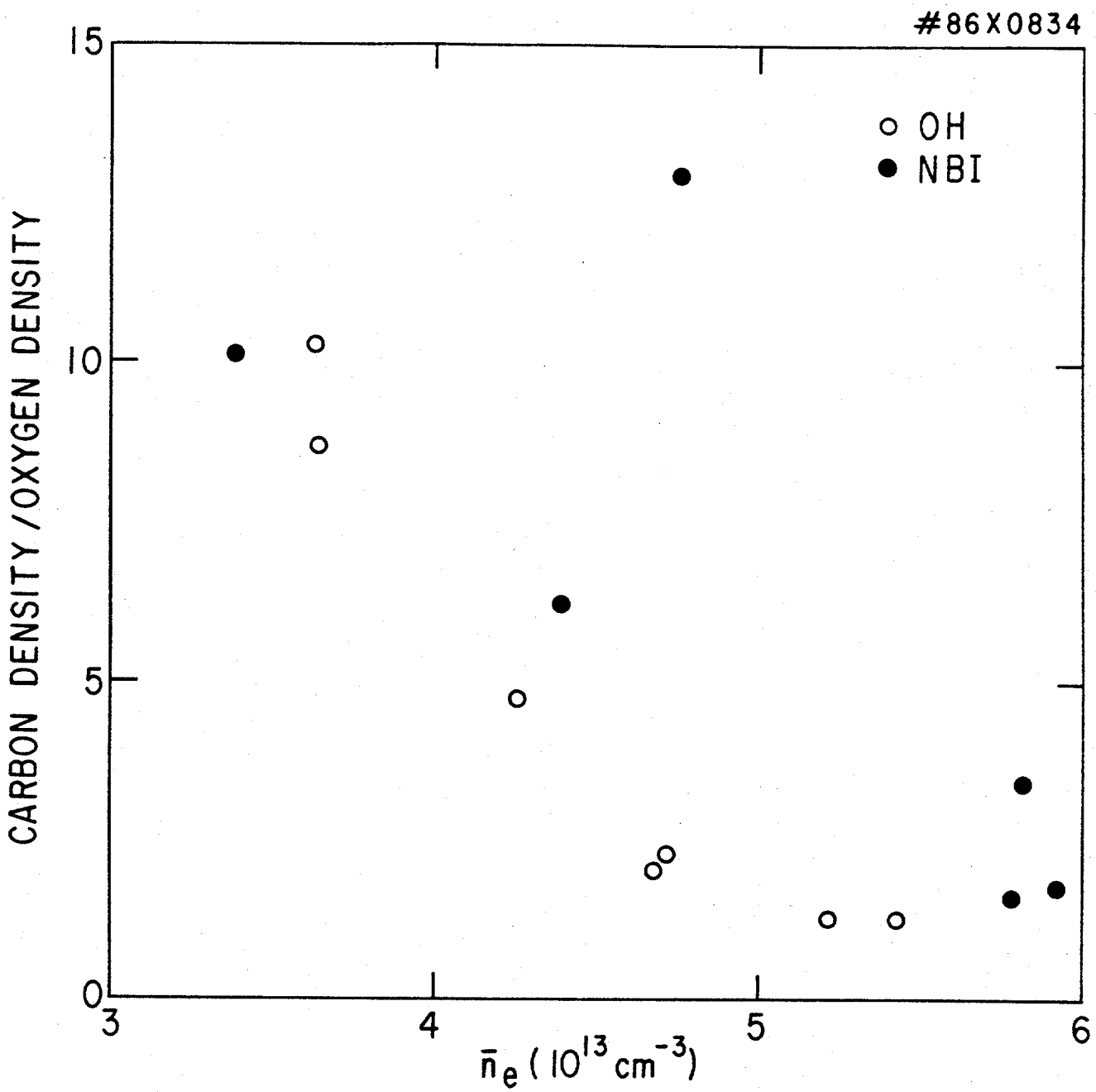
#86X0834
OH
NBI
CARBON DENSITY / OXYGEN DENSITY
15
10
5
0
3
4
5
6
$\bar{n}_e$ (10^{13} cm^{-3})

Fig. 11

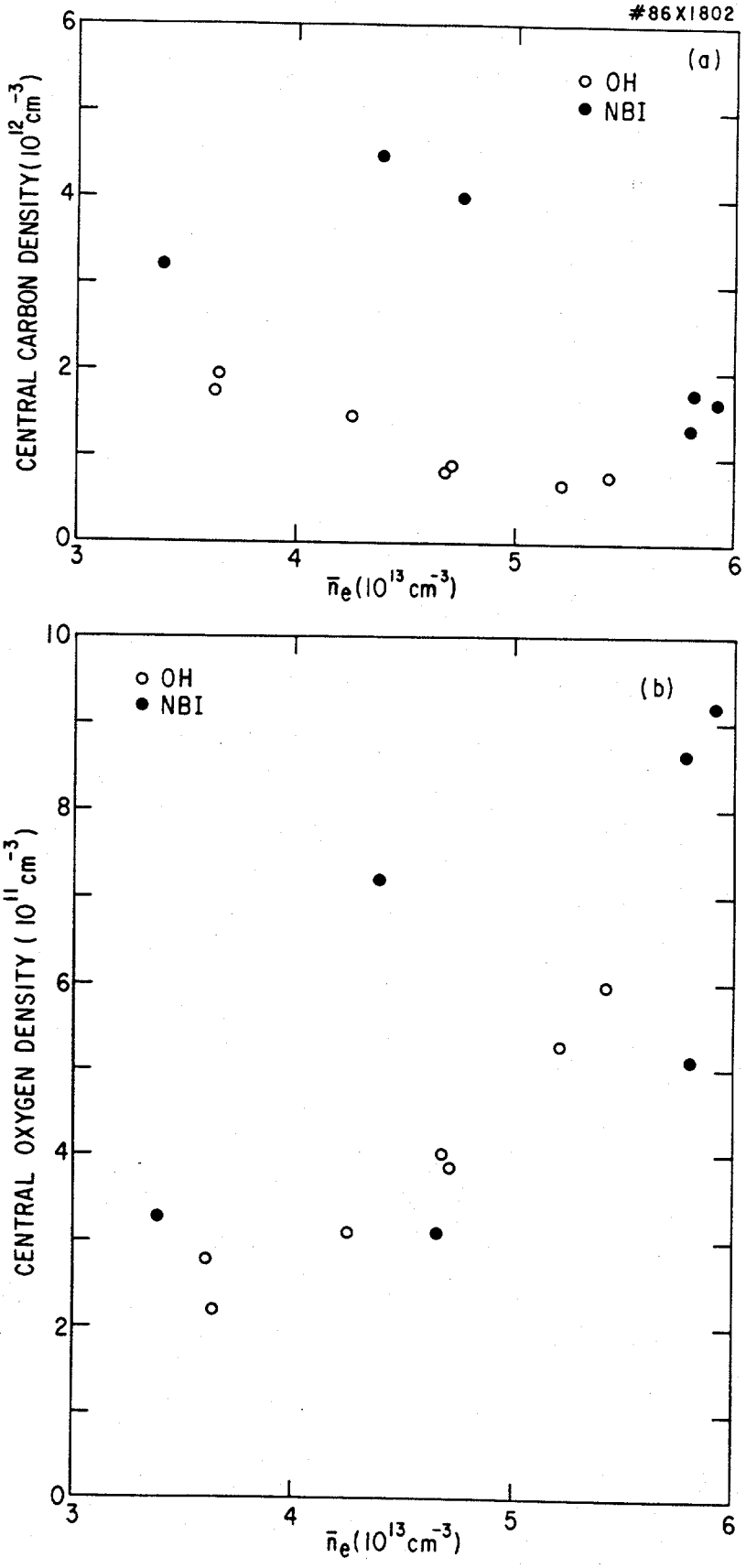
#86X1802
(a)
OH
NBI
CENTRAL CARBON DENSITY (10^{12} cm^{-3})
$\bar{n}_e$(10^{13} cm^{-3})
(b)
OH
NBI
CENTRAL OXYGEN DENSITY (10^{11} cm^{-3})
$\bar{n}_e$(10^{13} cm^{-3})

Fig. 12

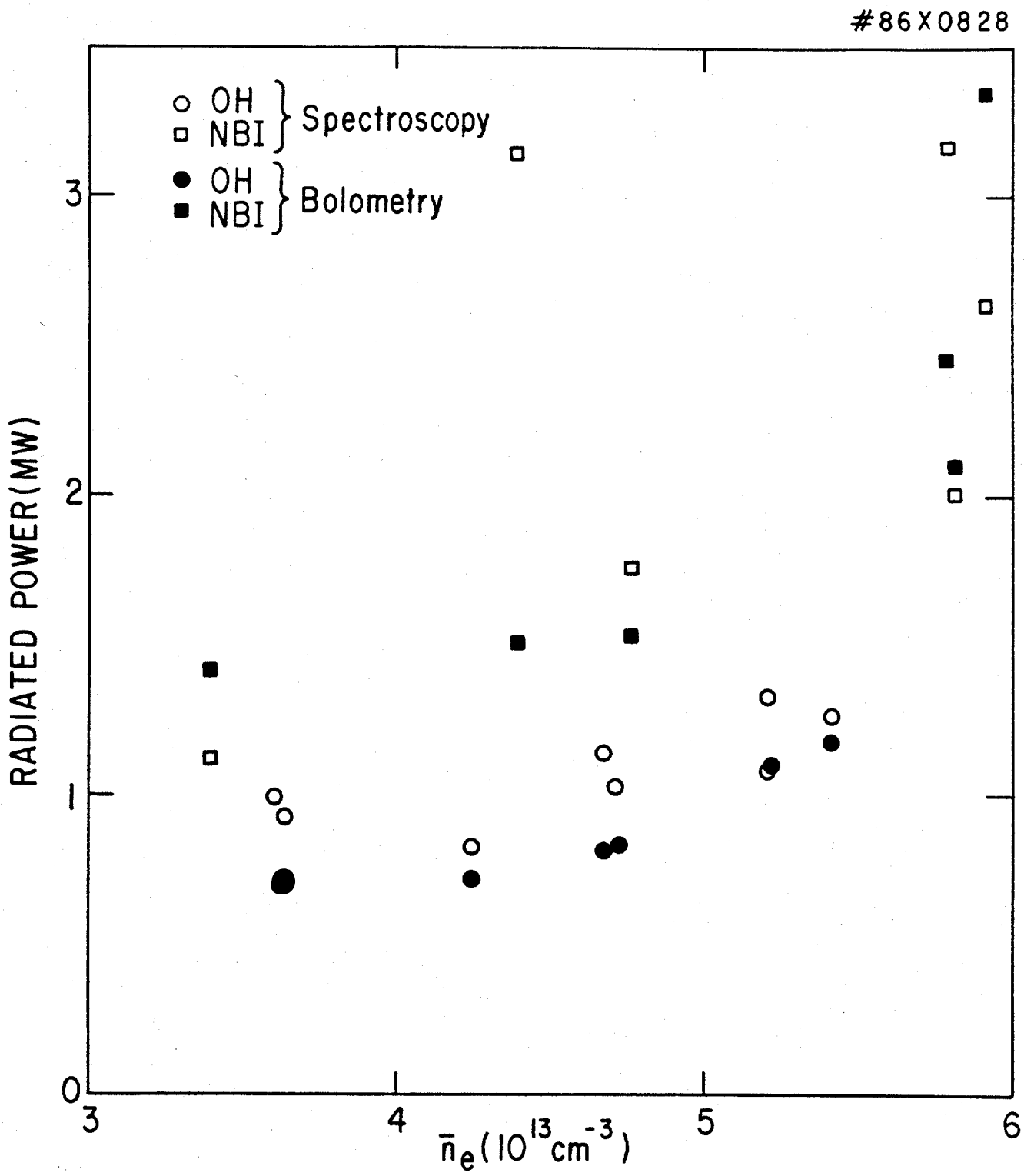
#86X0828
OH
NBI
Spectroscopy
OH
NBI
Bolometry
RADIATED POWER(MW)
0
1
2
3
3
4
5
6
$\bar{n}_e(10^{13}cm^{-3})$

Fig. 13

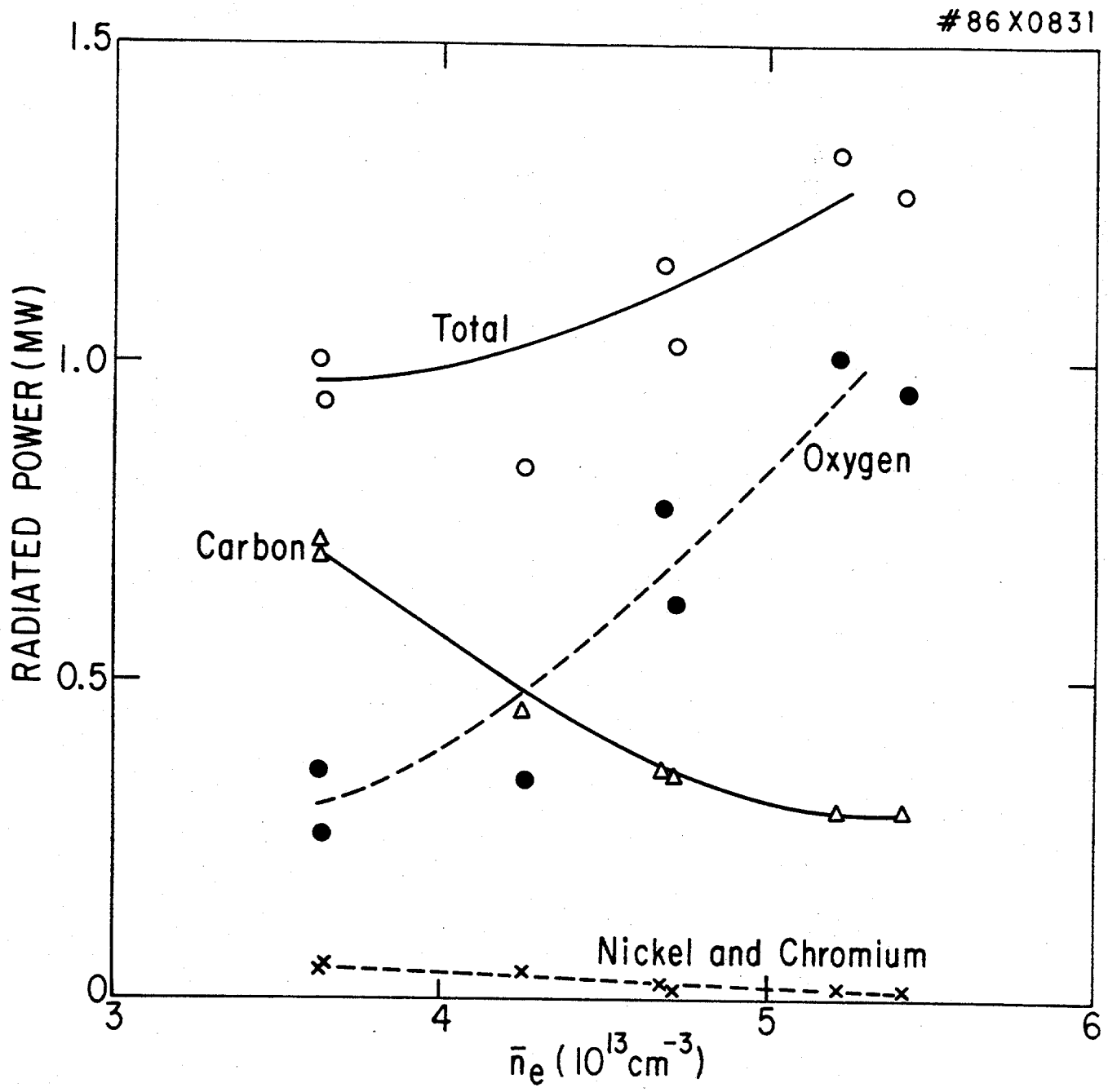
#86X0831
1.5
1.0
0.5
0
RADIATED POWER (MW)
Total
Oxygen
Carbon
Nickel and Chromium
3
4
5
6
$\bar{n}_e$ (10^{13}cm^{-3})

Fig. 14

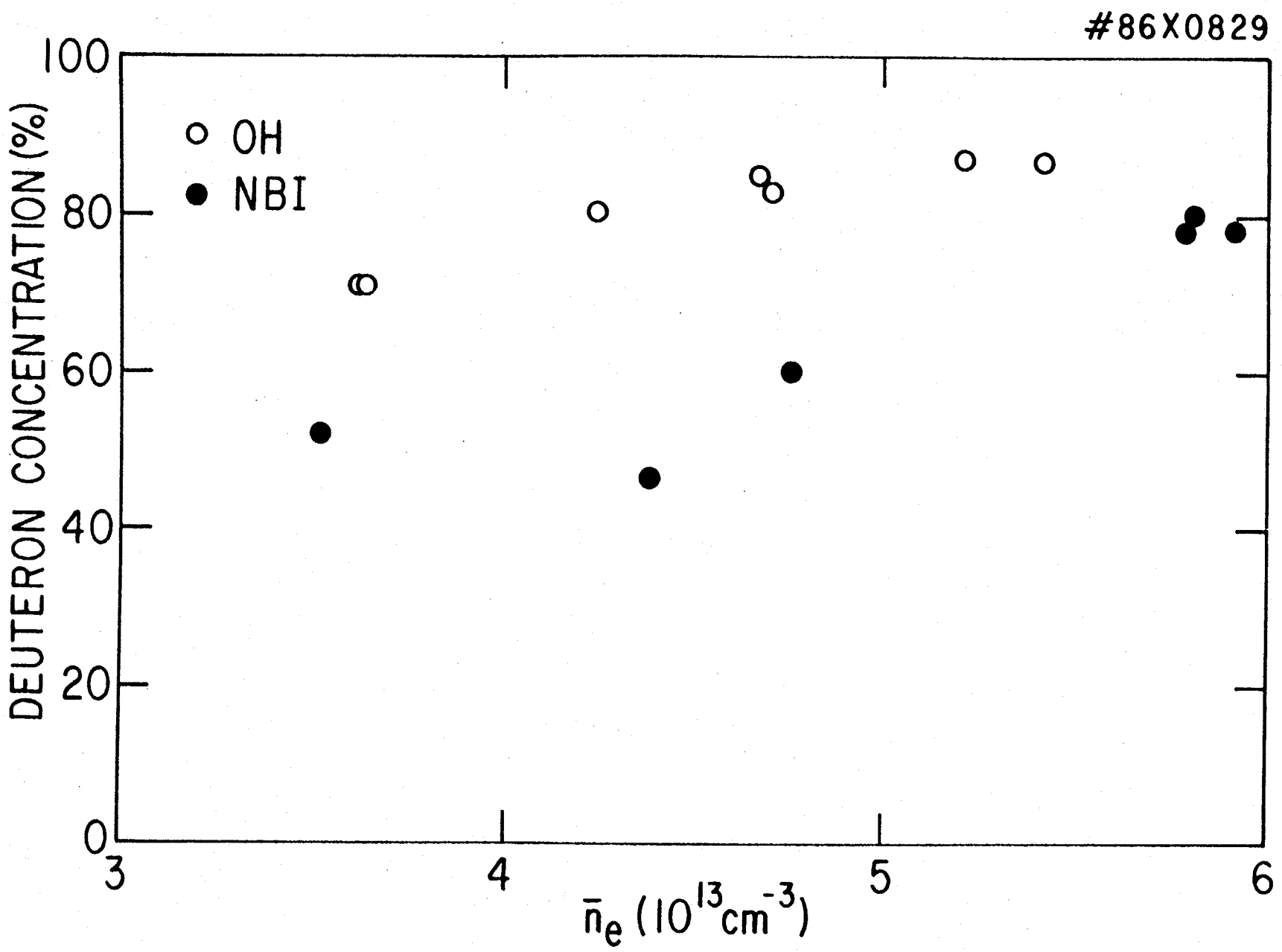
#86X0829
DEUTERON CONCENTRATION (%)
100
80
60
40
20
0
OH
NBI
3
4
5
6
$\bar{n}_e$ (10^{13}cm^{-3})

Fig. 15

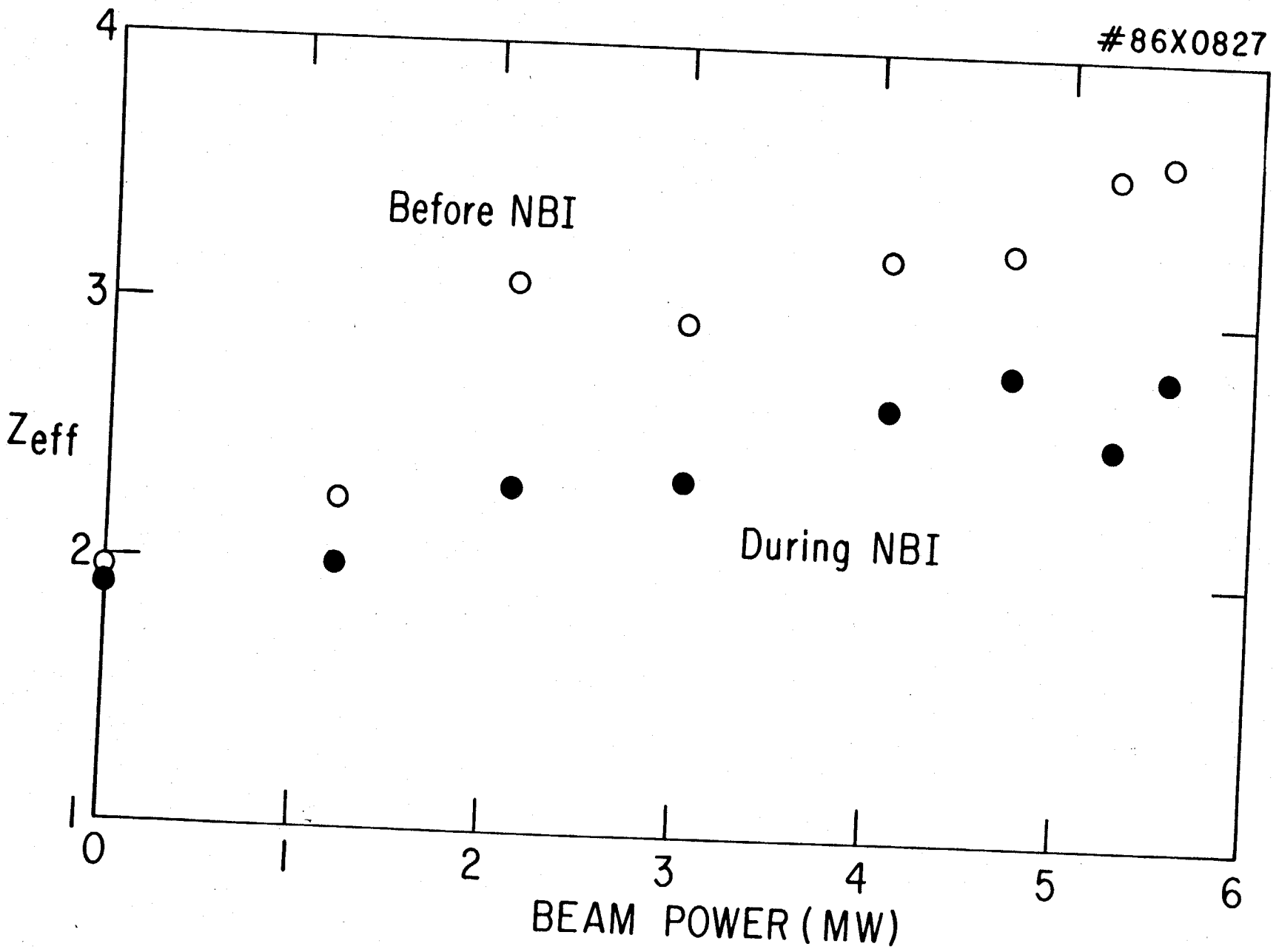
#86X0827
Before NBI
During NBI
Zeff
BEAM POWER (MW)
0
1
2
3
4
5
6
1
2
3
4

Fig. 16

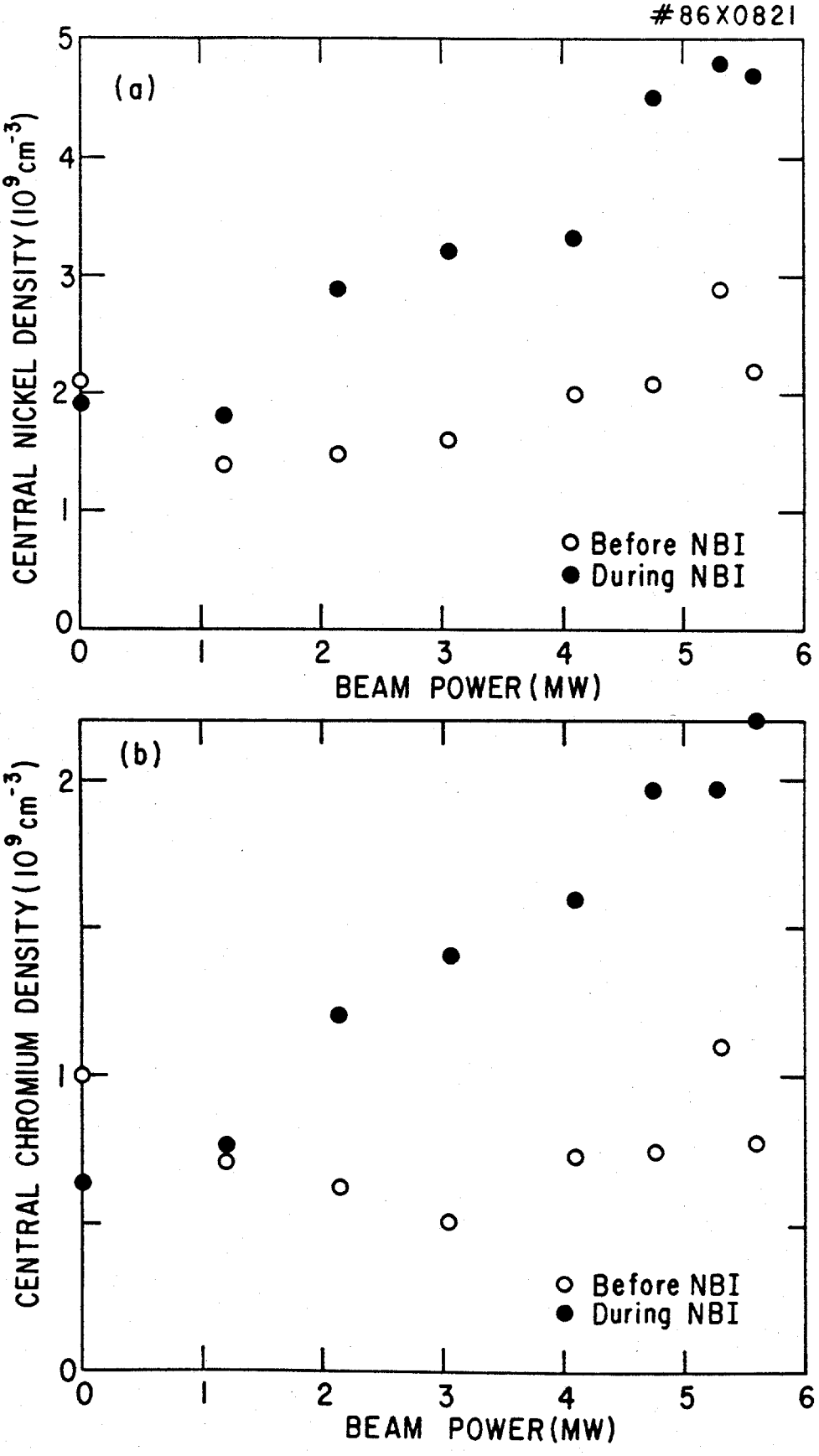
#86X0821
(a)
CENTRAL NICKEL DENSITY (10^9 cm^{-3})
BEAM POWER (MW)
Before NBI
During NBI
(b)
CENTRAL CHROMIUM DENSITY (10^9 cm^{-3})
BEAM POWER (MW)
Before NBI
During NBI

Fig. 17

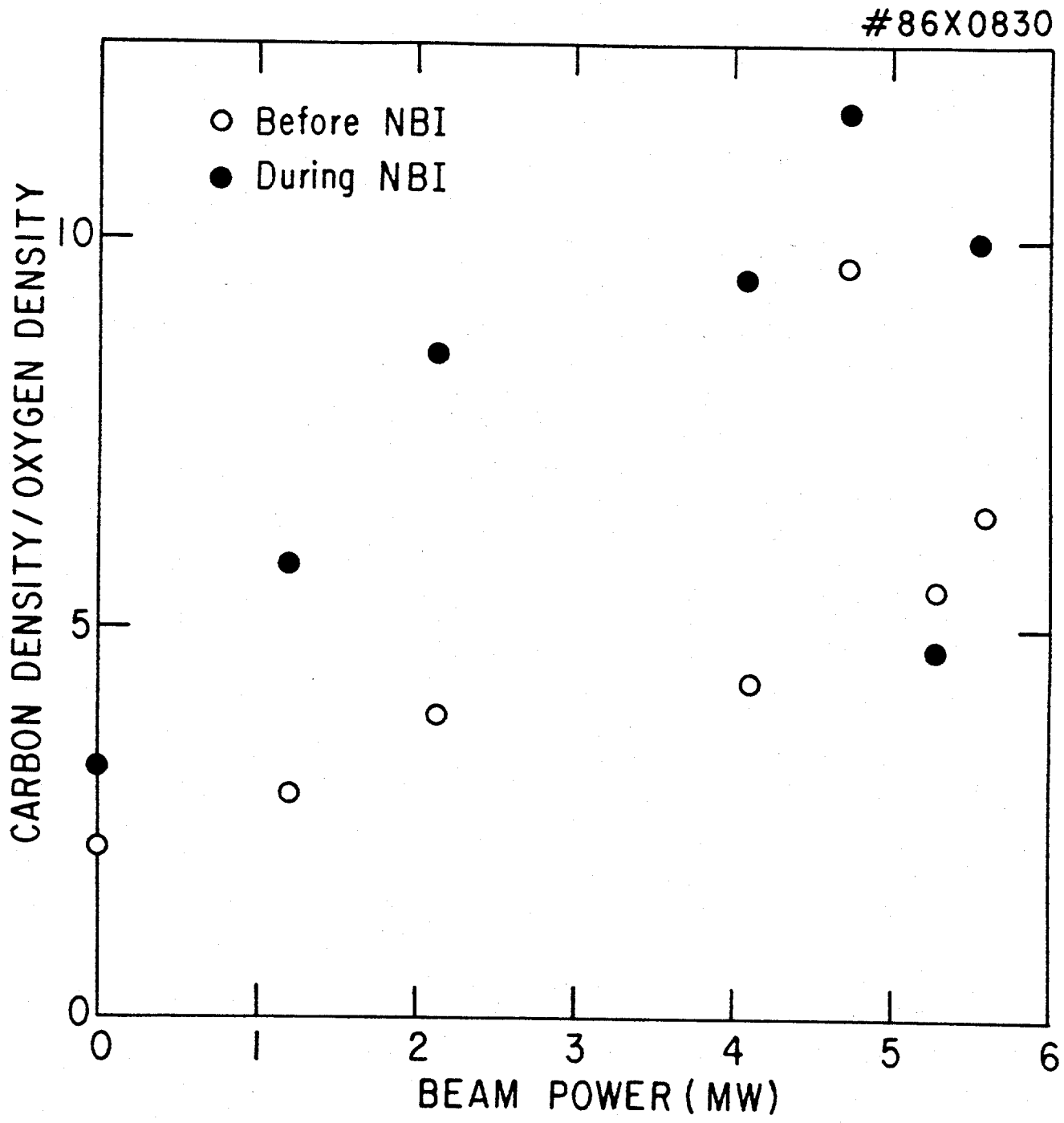
#86X0830
Before NBI
During NBI
CARBON DENSITY/OXYGEN DENSITY
10
5
0
0
1
2
3
4
5
6
BEAM POWER (MW)

Fig. 18

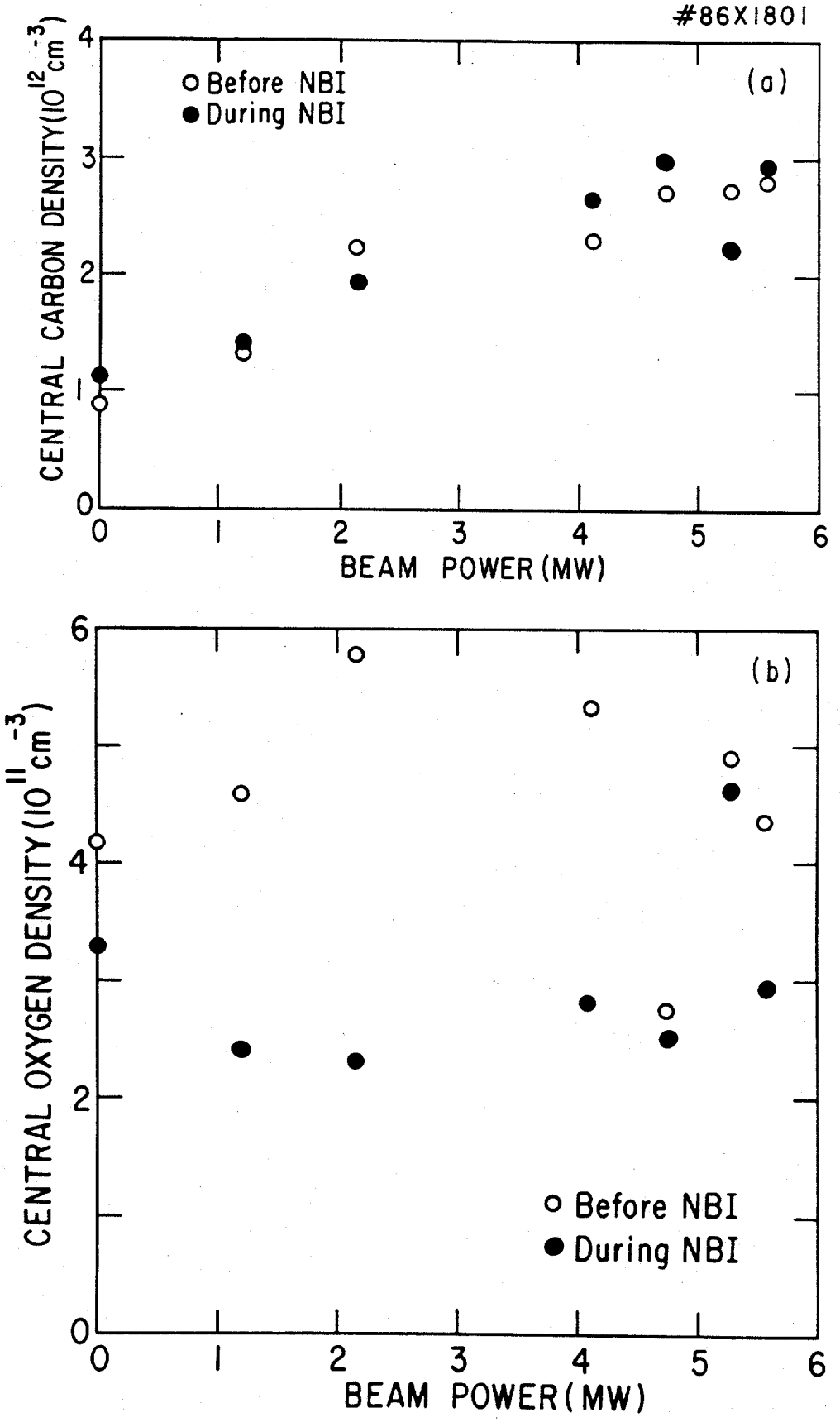
#86X1801
(a)
○ Before NBI
● During NBI
CENTRAL CARBON DENSITY(10^{12} cm^{-3})
BEAM POWER (MW)
(b)
CENTRAL OXYGEN DENSITY(10^{11} cm^{-3})
○ Before NBI
● During NBI
BEAM POWER (MW)

Fig. 19

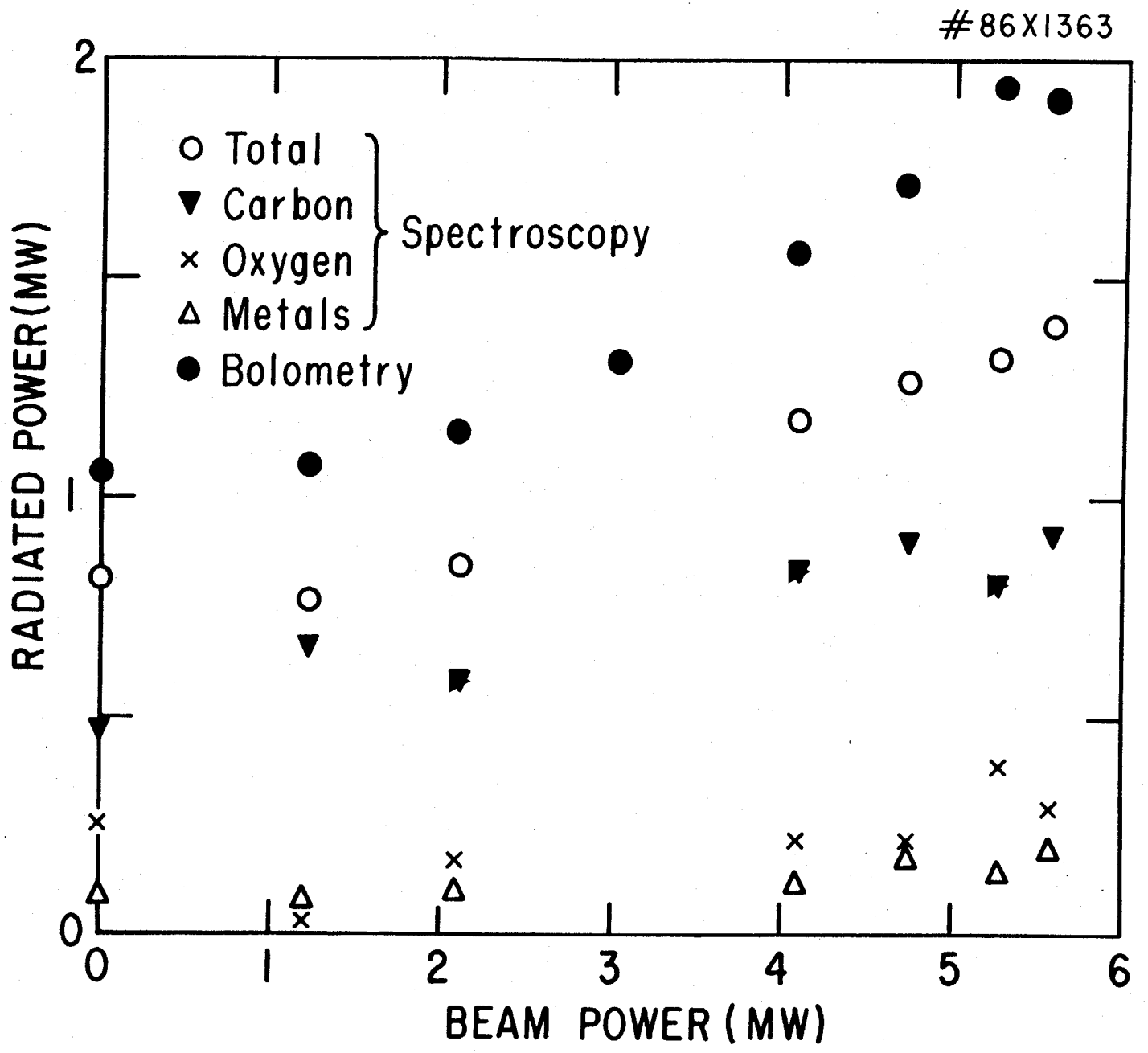
#86X1363
RADIATED POWER(MW)
BEAM POWER (MW)
Total
Carbon
Oxygen
Metals
Bolometry
Spectroscopy
0
1
2
3
4
5
6

Fig. 20

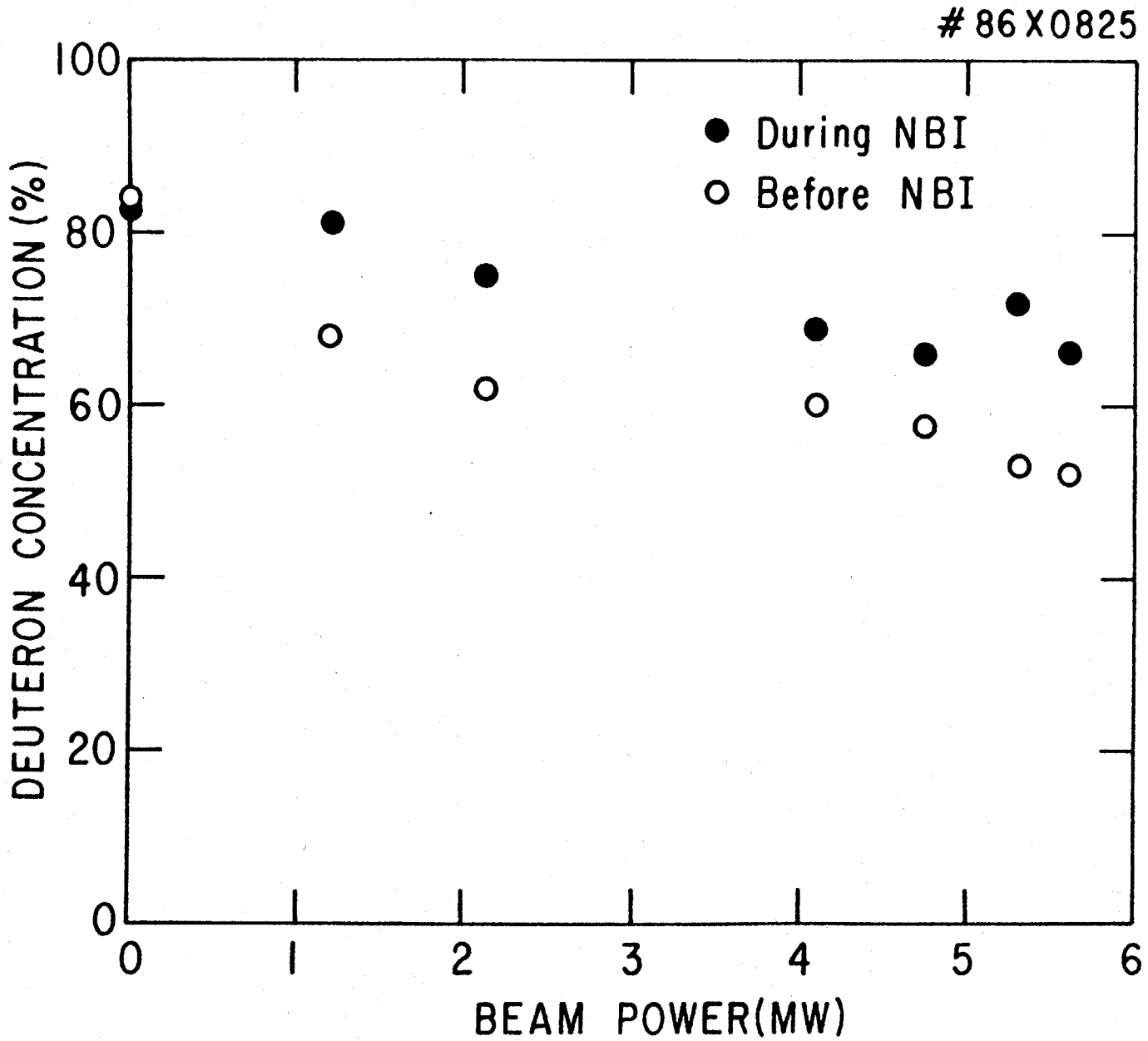
#86X0825
100
80
60
40
20
0
DEUTERON CONCENTRATION (%)
During NBI
Before NBI
0
1
2
3
4
5
6
BEAM POWER(MW)

Fig. 21